Chapter 5

Evolution of dwarf galaxies: a dynamical perspective

— **Federico Lelli, Filippo Fraternali, and Marc Verheijen** —

Submitted to Astronomy & Astrophysics

Abstract

For a rotating galaxy, the inner circular-velocity gradient $d_R V(0)$ provides a direct estimate of the central dynamical mass density, including gas, stars, and dark matter. We consider 60 low-mass galaxies with high-quality H I and/or stellar rotation curves (including starbursting dwarfs, irregulars, and spheroidals), and estimate $d_R V(0)$ as $V_{R_\mathrm{d}}/R_\mathrm{d}$, where R_d is the galaxy scale-length. For gas-rich dwarfs, we find that $V_{R_\mathrm{d}}/R_\mathrm{d}$ correlates with the central surface brightness μ_0, the mean atomic gas surface density Σ_gas, and the star formation rate surface density Σ_SFR. Starbursting galaxies, such as blue compact dwarfs (BCDs), generally have higher values of $V_{R_\mathrm{d}}/R_\mathrm{d}$ than dwarf irregulars, suggesting that the starburst is closely related to the inner shape of the potential well. There are, however, some "compact" irregulars with values of $V_{R_\mathrm{d}}/R_\mathrm{d}$ similar to BCDs. Unless a redistribution of mass takes place, BCDs must evolve into compact irregulars. Rotating spheroidals in the Virgo cluster follow the same correlation between $V_{R_\mathrm{d}}/R_\mathrm{d}$ and μ_0 as gas-rich dwarfs. They have values of $V_{R_\mathrm{d}}/R_\mathrm{d}$ comparable to those of BCDs and compact irregulars, pointing at evolutionary links between these types of dwarfs. Finally, we find that, similarly to spiral galaxies and massive starbursts, the star-formation activity in dwarfs can be parametrized as $\Sigma_\mathrm{SFR} = \epsilon\, \Sigma_\mathrm{gas}/\tau_\mathrm{orb}$, where τ_orb is the orbital time and $\epsilon \simeq 0.02$.

5.1 Introduction

Low-luminosity, dwarf galaxies are the most common systems in the Universe (e.g. Ferguson & Binggeli 1994). Despite numerous observational and theoretical studies, their formation and evolution is still not fully understood (e.g. Tolstoy et al. 2009; Mayer 2011; Kormendy & Bender 2012). Three main types of dwarfs exist in the nearby Universe: i) gas-poor dwarfs that are *not* currently forming stars, which are usually called spheroidals (Sphs) or dwarf ellipticals (dEs), hereafter we will refer to them as Sphs; ii) gas-rich dwarfs that are forming stars at a relatively-low rate, named irregulars (Irrs); and iii) starbursting dwarfs that are forming stars at an unusually high rate. The latter objects are often classified as amorphous dwarfs (based on optical morphology, e.g. Gallagher & Hunter 1987; Marlowe et al. 1999), H II-galaxies (based on emission-line spectroscopy, e.g. Terlevich et al. 1991), and/or blue compact dwarfs (BCDs, based on colors and surface brightness measurements, e.g. Gil de Paz et al. 2003). Hereafter, we will refer to any starbursting dwarf as a BCD. As we will show in Sect. 5.4.1, the term "BCD" captures a fundamental observational fact: the starburst activity (the *blue* color) occurs mainly in galaxies with a steep gravitational potential (i.e., a *compact* distribution of mass), providing that they have also a strong concentration of gas.

It is known that Sphs, Irrs, and BCDs follow the same correlations between the effective surface brightness $\mu_{\rm eff}$, the effective radius $R_{\rm eff}$, and the total magnitude M, pointing at evolutionary links between them (e.g. Kormendy 1985; Binggeli 1994; Tolstoy et al. 2009). In this respect, BCDs are particularly interesting as the burst durations are typically of the order of a few 100 Myr (McQuinn et al. 2010a), thus they must evolve into another type of dwarf as the starburst fades. The possibility of morphological transformations between low-mass galaxies is also suggested by the existence of "transition type" dwarfs, which have intermediate properties between Sphs and Irrs/BCDs (e.g. Sandage & Hoffman 1991; Mateo 1998; Dellenbusch et al. 2007, 2008).

Several photometric studies have shown that the underlying, old stellar component of BCDs typically has a smaller scale-length and a higher central surface brightness than Irrs and Sphs of the same luminosity, suggesting that the evolutionary links between BCDs and Irrs/Sphs are not straightforward (e.g. Papaderos et al. 1996; Gil de Paz & Madore 2005). However, it is generally difficult to obtain accurate structural parameters for starbursting dwarfs, as the galaxy morphology is extremely irregular and young stars may dominate the integrated light over much of the stellar body. Recently, Micheva et al. (2013) obtained deep optical and near-infrared photometry, and challenged the previous results, arguing that the structural parameters of the old stellar component of BCDs are consistent with those of Irrs and Sphs.

A different approach is to consider dynamical information that directly traces the distribution of mass, such as H I rotation curves (e.g. Lelli et al. 2012a,b). Using qualitative estimates of the rotation velocities, van Zee et al. (2001)

suggested that BCDs have steeper rotation curves than low surface brightness galaxies of similar luminosity (see also Meurer et al. 1998). In Chapter 3 (Lelli et al. 2012b), we considered a small sample of BCDs and Irrs with high-quality H I rotation curves, and measured the circular-velocity gradient $V_{R_\mathrm{d}}/R_\mathrm{d}$, where R_d is the exponential scale-length of the stellar body. We found that BCDs generally have higher values of $V_{R_\mathrm{d}}/R_\mathrm{d}$ than typical Irrs, implying that they have a higher central dynamical mass density (including gas, stars, and dark matter). BCDs also have higher central H I surface densities than Irrs (e.g. van Zee et al. 1998, 2001; Simpson & Gottesman 2000). This suggests that the starburst is closely related to the inner shape of the gravitational potential and to the central concentration of gas. This connection must be the key to understanding the mechanisms that trigger and drive the starburst in BCDs.

In this paper, we confirm the results of Lelli et al. (2012b) for a larger sample of BCDs and Irrs, and include star formation rate (SFR) indicators in the analysis. We also consider a sample of rotating Sphs. We use the dynamical information provided by $V_{R_\mathrm{d}}/R_\mathrm{d}$ to constrain the possible evolutionary links between dwarf galaxies.

5.2 The sample

We define a dwarf galaxy as an object with $V_\mathrm{flat} \leq 100$ km s^{-1}, where V_flat is the asymptotic velocity along the flat part of the rotation curve. For a pressure-supported system, V_flat can be estimated as $\sqrt{3}\sigma_\mathrm{obs}$ (McGaugh & Wolf 2010), where σ_obs is the observed velocity dispersion along the line of sight. According to the Tully-Fisher (TF) relation, $V_\mathrm{flat} \simeq 100$ km s^{-1} occurs at $M_\mathrm{B} \simeq -16.5$ mag (cf. Verheijen 2001), thus our definition of a dwarf galaxy qualitatively agrees with the standard one given by Tammann (1994), which is based on total luminosity and size. However, contrary to Tammann's criteria, our definition is directly related to the potential well of the galaxy and is not affected by the effects of recent star-formation, which can be serious for BCDs where the light is dominated by young stellar populations. The choice of 100 km s^{-1} is *not* arbitrary: in galaxies with $V_\mathrm{flat} \leq 100$ km s^{-1} bulges tend to disappear (e.g. Kormendy & Bender 2012) and some cosmological models predict that mass loss from supernova feedback may start to affect the baryonic content (e.g. Dekel & Silk 1986). Using the baryonic TF relation (e.g. McGaugh 2012), we estimate that galaxies with $V_\mathrm{flat} \leq 100$ km s^{-1} have a baryonic mass (stars and atomic gas) $M_\mathrm{bar} \lesssim 5 \times 10^9$ $M_\odot$.

We built a sample of dwarf galaxies with high-quality rotation curves, retrieving optical and H I data from various sources. We included in our selection also galaxies with rotation curves that do not reach the flat part but have $V_\mathrm{last} < 100$ km s^{-1}, where V_last is the circular velocity at the last measured point. The dynamical masses of these objects are uncertain, as their rotation curves may continue to rise, but their total magnitudes are $\lesssim -18$ R mag ($\lesssim -17$

B mag), indicating that these galaxies are actual dwarfs. In the following, we describe our sub-samples of starbursting dwarfs (BCDs), typical star-forming dwarfs (Irrs), and gas-poor dwarfs (Sphs). We also clarify the nomenclature used throughout this paper.

5.2.1 Starbursting dwarfs

In Chapter 4, we built a sample of 18 starbursting dwarfs by considering objects that satisfy two criteria: i) they have been resolved into single stars by the *Hubble Space Telescope* (HST); and ii) their star formation histories (SFHs), as derived by modelling color-magnitude diagrams (e.g. McQuinn et al. 2010a), show an increase in the recent SFR by a factor $\gtrsim 3$ with respect to the average, past SFR. We consider here a sub-sample of 8 objects, for which high-quality H I rotation curves could be derived (see Chapter 4). For another object (SBS 1415+437), we could derive a rotation curve but this may not be a reliable tracer of the gravitational potential, as the galaxy strongly deviates from the baryonic TF relation (see Fig. 8 in Chapter 4), thus we exclude this object here. As we stressed in Sect. 5.1, we refer to any starbursting dwarf as a BCD.

We also added the well-studied BCD NGC 2915, which has been resolved into single stars by HST (Karachentsev et al. 2003), but its SFH has not yet been derived. NGC 2915 has a regularly-rotating H I disk (Elson et al. 2010), but the inner parts of the rotation curve are uncertain because of the presence of strong non-circular motions (Elson et al. 2011), thus we assigned a conservative error of 15 km s^{-1} to the inner points of the rotation curve.

The properties of our sample of 9 BCDs are given in Tables 5.B.1 and 5.B.2. For all these objects, the HST studies provide accurate distances using the tip of the red giant branch (TRGB) method.

5.2.2 Irregulars

We selected 37 Irrs from the sample of Swaters et al. (2009). We required that the galaxies have high-quality rotation curves ($q \leq 2$, see Swaters et al. 2009) and inclinations between 30° and 80°, thus the rotation velocities and the central surface brightnesses can be measured with small uncertainties. The rotation curves of these galaxies have been derived by Swaters et al. (2009) taking into account beam-smearing effects. We also added another 6 objects that meet our quality-criteria: UGC 6955 (DDO 105) and UGC 8320 (DDO 168) from Broeils (1992), UGC 6399 and UGC 6446 from Verheijen & Sancisi (2001), and the Local Group dwarfs WLM (Jackson et al. 2004) and NGC 6822 (Weldrake et al. 2003). These 43 galaxies are classified as Irr, Im, Sm, or Sd (de Vaucouleurs et al. 1991); for simplicity we refer to all of them as Irr.

It is possible that some of these Irrs may harbour a starburst and, thus, should be considered as BCDs. For example, the sample of Swaters et al. (2009) contains NGC 4214 (IBm), NGC 2366 (IBm), and NGC 4068 (Im), which are part of our sample of starbursting dwarfs. Moreover, McQuinn et al. (2010a) studied the SFH of NGC 6822, a prototype Irr in the Local Group, and found that it may have experienced a recent starburst. However, since the HST field-of-view covers only ~10% of the stellar body of NGC 6822 (McQuinn et al. 2012), the SFH is representative of a small fraction of the galaxy, thus we prefer to consider NGC 6822 as a typical Irr (see also Mateo 1998; Tolstoy et al. 2009). The sample of Swaters et al. (2009) also contains Holmberg II (UGC 4305), which is a well-studied starbursting dwarf (Weisz et al. 2008; McQuinn et al. 2010b). For this galaxy, the value of the inclination i is uncertain: Swaters et al. (2009) assumed $i = 40^{\circ}$, Oh et al. (2011) derived $i = 49^{\circ}$ from a tilted-ring fit to the velocity field and $i = 25^{\circ}$ from the baryonic TF relation, whereas Gentile et al. (2012) constrained the outer value of i between 20° and 35° by building 3-dimensional disk models. Given these uncertainties, we chose to exclude Holmberg II.

Tables 5.B.3 and 5.B.4 provide the properties of our sample of 43 Irrs. Galaxy distances have been taken from the literature adopting the following distance indicators (in order of decreasing priority): Cepheids, TRGB, and TF relation.

5.2.3 Rotating spheroidals

The sample of gas-poor dwarfs is drawn from van Zee et al. (2004a,b), who used long-slit optical spectroscopy to derive stellar rotation curves and velocity dispersion profiles of 16 low-luminosity galaxies in the Virgo cluster. We selected only 8 objects that show a clear rotation-velocity gradient for $R \lesssim R_{\rm d}$. These galaxies have been classified as dEs by Binggeli et al. (1985). Following Kormendy et al. (2009), we refer to them as Sphs, since they are intrinsically different from bright elliptical galaxies and follow different scaling relations. We assume that the Virgo cluster is at a distance of 16.1±1.2 Mpc (Kelson et al. 2000).

Van Zee et al. (2004b) provide the rotation velocities projected along the line of sight. To trace the gravitational potential of the galaxy, these velocities must be corrected for inclination and pressure-support. To correct for inclination, we modelled the Sphs as thick disks (see Sect. 5.3.2). To correct for pressure-support, we calculated the asymmetric-drift correction (see Appendix 5.A). These 8 objects have $V_{\rm last} \leq 100$ km s^{-1} after applying the inclination and asymmetric-drift corrections, thus they fulfill our definition of a dwarf galaxy. The properties of our sample of rotating Sphs are given in Table 5.B.5.

5.3 Data Analysis

In Sect. 5.4, we will present several diagrams that compare the dynamical, structural, and star-formation properties of dwarf galaxies. Here we describe the quantities that enter in those diagrams and provide details about the error budget.

5.3.1 The circular-velocity gradient

The key quantity here is the inner circular-velocity gradient

$$d_R V(0) = \lim_{R \to 0} \frac{dV_{\rm circ}(R)}{dR}, \tag{5.1}$$

where $V_{\rm circ}(R)$ is the circular velocity of a test particle orbiting at the galactocentric radius R (see also Lelli et al. 2013). For a spherical distribution of mass, $d_R V(0) = \sqrt{4/3 \pi G \rho_0}$ where G is Newton's constant and ρ_0 is the central dynamical mass density (including gas, stars, and dark matter). Thus, for a given dynamical mass, $d_R V(0)$ provides, to a first approximation, a direct measure of the *inner steepness* of the potential well of a galaxy. The rotation curves of dwarf galaxies are typically described by a nearly solid-body part for $R \lesssim 2R_{\rm d}$ (where $R_{\rm d}$ is the exponential scale-length) and an outer flat part for $R \gtrsim 2R_{\rm d}$ (e.g. Swaters et al. 2009). Thus, we can estimate $d_R V(0)$ on the solid-body portion of the rotation curve as $V_{R_{\rm d}}/R_{\rm d}$, where $V_{R_{\rm d}} = V_{\rm circ}(R_{\rm d})$. If high-resolution rotation curves are available, it is possible to quantify $d_R V(0)$ using more sophisticated techniques such as a polynomial fit (Lelli et al. 2013); for bulgeless galaxies with a nearly-exponential luminosity profile, this would result in differences in $d_R V(0)$ within a factor of ∼2. For the purposes of this paper, a simple estimate of $d_R V(0)$ as $V_{R_{\rm d}}/R_{\rm d}$ is sufficiently accurate. We also note that, since we are considering the solid-body portion of the rotation curve, the exact value of $R_{\rm d}$ does not strongly affect the value of $d_R V(0) \simeq V_{R_{\rm d}}/R_{\rm d}$.

For gas-rich galaxies (BCDs and Irrs), $V_{\rm circ}(R)$ is directly provided by the H I rotation curve $v_{\rm rot}(R)$, as the asymmetric-drift correction to account for the pressure support is typically negligible in the inner galaxy regions (e.g. Swaters et al. 2009; Lelli et al. 2012b). For gas-poor galaxies (Sphs), instead, the stellar rotation curves must be corrected for pressure support. The asymmetric-drift correction is described in Appendix 5.A.

To estimate the error $\delta_{V/R}$ on $V_{R_{\rm d}}/R_{\rm d}$, we consider the following equation:

$$\frac{V_{\rm circ}}{R} = \frac{v_{\rm l.o.s}}{\sin(i)} \frac{1}{\alpha D}, \tag{5.2}$$

where $v_{\rm l.o.s}$ is the circular-velocity projected along the line of sight, i is the inclination, α is the angular scale-length (in radians), and D is the galaxy distance. The propagation of the errors gives

$$\delta^2_{V/R} = \left\{ \left[\frac{\delta_{v_{\rm l.o.s}}}{R \sin(i)} \right]^2 + \left[\frac{V_{\rm circ}}{R} \frac{\delta_i}{\tan(i)} \right]^2 + \left[\frac{V_{\rm circ}}{R} \frac{\delta_D}{D} \right]^2 \right\}_{R=R_{\rm d}} \tag{5.3}$$

where the error on α has been neglected. For $\delta_{v_{\rm l.o.s}}/\sin(i)$ we used the error on the rotation velocities given in the original papers; this includes the formal error given by a χ^2-minimization and an additional uncertainty due to the asymmetries between the approaching and the receding side of the galaxy (see e.g. Swaters et al. 2009). For δ_i we assumed a typical error of 3°, as δ_i is not provided in the original papers (except in a few cases, see Tables 5.B.1 and 5.B.3). Typically, δ_D gives a negligible contribution for galaxies with Cepheids and TRGB distances, whereas it dominates the error budget for galaxies with TF distances.

5.3.2 Structural parameters

We collected R-band apparent magnitudes $m_{\rm R}$, central surface brightnesses μ_0, and scale-lengths $R_{\rm d}$ from various sources. For the BCDs, we refer to Chapter 4. For the Irrs, the sources are Swaters & Balcells (2002) (40 galaxies), Tully et al. (1996) (UGC 6399 and UGC 6446), and Hunter & Elmegreen (2006) (WLM and NGC 6822, their V-band values have been converted to R-band assuming $V-R=0.5$). For the Sphs, the source is van Zee et al. (2004a). These authors derived the structural parameters μ_0 and $R_{\rm d}$ by fitting an exponential function to the outer parts of the surface brightness profiles. For BCDs, the resulting values of μ_0 and $R_{\rm d}$ are thought to be representative of the underlaying, old stellar component (e.g. Papaderos et al. 1996; Gil de Paz & Madore 2005).

We calculated absolute magnitudes $M_{\rm R}$ using our adopted distances, and estimated the errors considering the distance uncertainties only, hence $\delta_M = 5\log(e)\delta_D/D$. We corrected μ_0 for inclination i using the following equation:

$$\mu_0^i = \mu_0 - 2.5C\log[\cos(i)] \tag{5.4}$$

where C is a constant related to the internal extinction. Since dwarf galaxies typically have low metallicities (see Tables 5.B.2 and 5.B.4), the dust content is likely low. Hence, we assumed that they are optically-thin ($C=1$). The error $\delta_{\mu_0^i}$ on μ_0^i is given by:

$$\delta^2_{\mu^i} = \delta^2_{\mu_0} + [2.5\log(e)\tan(i)\delta_i]^2. \tag{5.5}$$

Since δ_{μ_0} is usually not provided in the original papers, we assumed that $\delta_{\mu_0} = 0.1$ mag. This conservative choice takes into account uncertainties on the photometric calibration, on the exponential fits, and on the fact that the surface brightness profiles of dwarf galaxies may have inner cores or cusps (see e.g. Swaters & Balcells 2002).

For BCDs and Irrs, the inclination was derived by fitting a tilted-ring model to the H I velocity field and/or by building model-cubes (see Chapter 4 and Swaters et al. 2009 for details). For Sphs, we estimated i from the observed ellipticities ε using the formula

$$\cos i^2 = \frac{(1-\varepsilon)^2 - q_0^2}{1-q_0^2}, \tag{5.6}$$

where q_0 is a constant that depends on the oblateness of the stellar distribution. We assumed $q_0 = 0.35$, as indicated by statistical studies of the observed ellipticities of dwarf galaxies (Lisker et al. 2007; Sánchez-Janssen et al. 2010). If one assumes that $q_0 = 0.2$, a typical value for the stellar disks of spiral galaxies (e.g. Holmberg 1950), the difference in i would be $\lesssim 3°$ for $\varepsilon \leq 0.35$ (within our assumed error δ_i) and $\lesssim 6°$ for $0.35 < \varepsilon < 0.55$ (within $2\delta_i$). In our sample of Sphs, there are no objects with $\varepsilon > 0.55$. Our results are listed in Tables 5.B.1, 5.B.3, and 5.B.5.

5.3.3 Gas and star formation properties

We collected information about the H I content, ionized-gas metallicity, and star formation for all the BCDs and Irrs in our sample. These are briefly described in the following.

We calculated H I masses using the standard formula

$$M_{\rm H\,I}\,[M_\odot] = 236 \times D\,[\rm Mpc]^2 \times S_{\rm H\,I}\,[\rm mJy\,km\,s^{-1}], \tag{5.7}$$

where $S_{\rm H\,I}$ is the observed H I flux from interferometric 21-cm line observations. The error $\delta_{M_{\rm H\,I}}$ on $M_{\rm H\,I}$ is given by:

$$\delta^2_{M_{\rm H\,I}} = (472\,D\,S_{\rm H\,I}\,\delta_D)^2 + (236\,D^2\,\delta_{S_{\rm H\,I}})^2. \tag{5.8}$$

Since the error on $S_{\rm H\,I}$ is usually not given in the original papers, we assumed $\delta_{S_{\rm H\,I}} = 0.1\,S_{\rm H\,I}$ (the typical calibration error of standard H I observations).

Following Swaters et al. (2002), we define the optical radius $R_{\rm opt} = 3.2R_{\rm d}$. $R_{\rm opt}$ is *not* an isophotal radius and, thus, allows us to compare the sizes of galaxies with different central surface brightnesses. For a HSB exponential disk with $\mu_0(B) = 21.65$ mag (Freeman 1970), $R_{\rm opt} = 3.2\ R_{\rm d}$ is equivalent to the usual isophotal radius R_{25}. We define $\overline{\Sigma}_{\rm H\,I}$ as the mean H I surface density within $R_{\rm opt}$. $\overline{\Sigma}_{\rm H\,I}$ is derived from the observed H I map using an elliptical aperture, and is corrected for i by multiplying the mean H I column density $\overline{N}_{\rm H\,I}$ by $\cos(i)$. We calculated $\overline{\Sigma}_{\rm H\,I}$ for our sample of BCDs, while Swaters et al. (2002) provide $\overline{\Sigma}_{\rm H\,I}$ for 38 Irrs. We point out that $\overline{\Sigma}_{\rm H\,I}$ is distance-independent and nearly unaffected by the linear resolution (in kpc) of the H I observations, as the galaxies in our sample are resolved within $R_{\rm opt}$. The error $\delta_{\overline{\Sigma}_{\rm H\,I}}$ on $\overline{\Sigma}_{\rm H\,I}$ is given by

$$\delta^2_{\overline{\Sigma}_{\rm H\,I}} = [\cos(i)\delta_{\overline{N}_{\rm H\,I}}]^2 + [\overline{N}_{\rm H\,I}\sin(i)\delta_i]^2 \tag{5.9}$$

where $\delta_{\overline{N}_{\rm H\,I}}$ is assumed to be 10% of $\overline{N}_{\rm H\,I}$.

We calculated SFRs using the Hα luminosities $L_{\rm H\alpha}$ from Kennicutt et al. (2008), scaled to our assumed distances, and the standard calibration from Kennicutt (1998a). This calibration assumes a Salpeter initial mass function (IMF) from 0.1 to 100 $\rm M_\odot$ and solar metallicity. The latter assumption is clearly not valid for dwarf galaxies, which generally have sub-solar metallicities (see Tables 5.B.1 and 5.B.4). According to Lee et al. (2009), the ratio SFR/$\mathrm{L}_{\mathrm{H}\alpha}$ for a galaxy with $Z \simeq Z_{\odot}/5$ is a factor of ∼0.7 lower with respect to a galaxy with $Z = Z_{\odot}$, thus our SFRs may be slightly overestimated. Other common calibrations, which assume a Kroupa IMF and different stellar evolutionary models, would give SFRs that are lower by a factor of ∼0.68 (see Kennicutt & Evans 2012). Kennicutt et al. (2008) provides $L_{\mathrm{H}\alpha}$ for 8 BCDs and 29 Irrs present in our sample. For the remaining BCD (I Zw 18), we used the Hα luminosity from Gil de Paz et al. (2003). For another 8 Irrs, we used the Hα SFRs calculated by James et al. (2004) (scaled to our assumed distances and uncorrected for internal extiction), who also used the Kennicutt (1998a) calibration. Besides the uncertainties on the absolute SFR calibration, the errors on the SFRs are of the order of $2\delta_D/D$.

We then calculated the SFR surface density $\Sigma_{\mathrm{SFR}} = \mathrm{SFR}/(\pi R_{\mathrm{opt}}^2)$ and the ratio SFR/M_{bar}, which is a baryonic version of the specific SFR (sSFR=SFR/M_*). The baryonic mass (stars and atomic gas) was estimated from the baryonic TF relation, calibrated by McGaugh (2012) as $M_{\mathrm{bar}}[M_{\odot}] = 47 \times V_{\mathrm{circ}}^4[\mathrm{km\,s^{-1}}]$ with an accuracy of ∼10%. For the 16 Irrs and 2 BCDs that do not reach the flat part of the rotation curve, this baryonic mass may be slightly underestimated. We also calculated two types of gas-depletion times: i) $\tau_{\mathrm{global}} = 1.33\,M_{\mathrm{H\,I}}/\mathrm{SFR}$, which considers the total atomic gas mass, and ii) $\tau_{\mathrm{local}} = 1.33\,\overline{\Sigma}_{\mathrm{H\,I}}/\Sigma_{\mathrm{SFR}}$, which considers only the atomic gas mass inside R_{opt}. The factor 1.33 takes into account the contribution of Helium. Note that Σ_{SFR}, τ_{global}, and τ_{local} are distance independent; the errors depend on the accuracy of the H I and Hα flux calibrations (typically ∼10%) and on the SFR calibration. Since the SFRs may be *overestimated* up to a factor of ∼2 due to the assumptions on the IMF and metallicity, the gas depletion times may be slightly *underestimated*. Finally, we compiled Hα+[N II] equivalent widths (EW) and ionized-gas metallicities $12 + \log(O/H)$ from the literature. Our results are listed in Tables 5.B.2 and 5.B.4.

5.4 Results

5.4.1 Gas-rich dwarf galaxies

We start by comparing the dynamical properties of gas-rich, star-forming dwarfs (BCDs and Irrs). As discussed in Sect. 5.3.1, for a bulgeless galaxy with a nearly exponential luminosity profile, $V_{R_{\mathrm{d}}}/R_{\mathrm{d}}$ is a good proxy for the circular-velocity gradient $d_R V(0) \propto \sqrt{\rho_0}$, where ρ_0 is the central dynamical mass density (including gas, stars, and dark matter). In Fig. 5.1, $V_{R_{\mathrm{d}}}/R_{\mathrm{d}}$ is plotted versus the central surface brightness μ_0^i (left) and the mean H I surface density $\overline{\Sigma}_{\mathrm{H\,I}}$ (right). $V_{R_{\mathrm{d}}}/R_{\mathrm{d}}$ correlates with both μ_0^i and $\overline{\Sigma}_{\mathrm{H\,I}}$ (see also Lelli et al. 2012b, 2013). Gas-rich dwarfs with a high central dynamical mass density (high $V_{R_{\mathrm{d}}}/R_{\mathrm{d}}$)

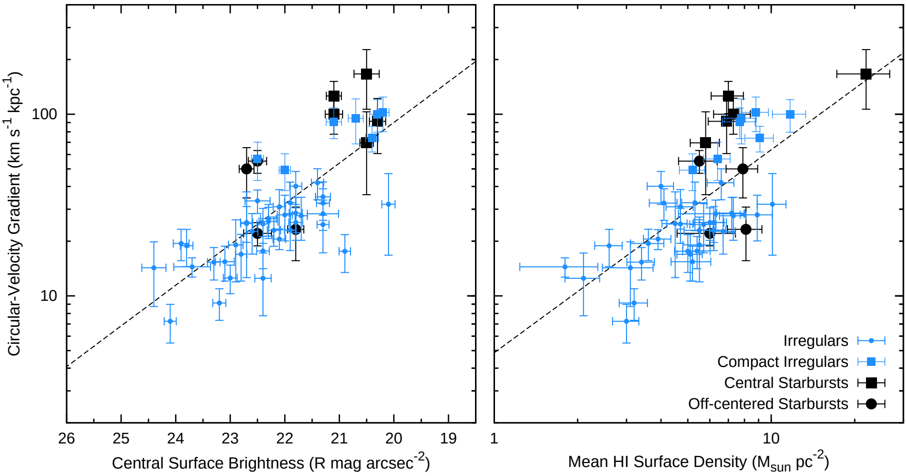

Figure 5.1 – *Left:* the circular-velocity gradient $V_{R_\mathrm{d}}/R_\mathrm{d}$ versus the R-band central surface brightness (inclination corrected). *Right:* $V_{R_\mathrm{d}}/R_\mathrm{d}$ versus the mean H I surface density within R_opt. The black dots and squares show, respectively, BCDs with a diffuse/off-centered starburst and BCDs with a centrally-concentrated starburst. The blue dots and squares show, respectively, typical Irrs and compact Irrs. The dashed lines show a linear-fit to the data. See Sect. 5.4.1 for details.

have also a high central surface brightness and a high H I surface density within the stellar body. To quantify the statistical significance of these relations, we calculated the Pearson's correlation coefficient ρ_cc, where $\rho_\mathrm{cc} = \pm 1$ for an ideal linear correlation/anticorrelation, while $\rho_\mathrm{cc} = 0$ if no correlation is present. We found that both correlations are highly significant: the $V_{R_\mathrm{d}}/R_\mathrm{d} - \mu_0^i$ diagram has $\rho_\mathrm{cc} \simeq -0.8$, while the $V_{R_\mathrm{d}}/R_\mathrm{d} - \overline{\Sigma}_\mathrm{H\,I}$ diagram has $\rho_\mathrm{cc} \simeq 0.7$. A linear, error-weighted fit to the data returns

$$\log(V_{R_\mathrm{d}}/R_\mathrm{d}) = (-0.22 \pm 0.03)\,\mu_0^i + (6.4 \pm 0.6), \tag{5.10}$$

and

$$\log(V_{R_\mathrm{d}}/R_\mathrm{d}) = (1.1 \pm 0.2)\,\log(\overline{\Sigma}_\mathrm{H\,I}) + (0.7 \pm 0.1). \tag{5.11}$$

The left panel of Fig. 5.1 is nearly equivalent to the lower part of the scaling relation described in Chapter 7 (Lelli et al. 2013), which holds for both irregular and spiral galaxies and extends for 2 orders of magnitude in $d_R V(0)$ and 4 orders of magnitude in surface brightness. The values of the slope and intersect in Eq. 5.10 are in close agreement with those found in Lelli et al. (2013) (-0.22 ± 0.02 and 6.3 ± 0.4, respectively).

The previous correlations are completely driven by the *local*, inner properties of the galaxies (μ_0^i and $\overline{\Sigma}_\mathrm{H\,I}$) and not by *global* properties, such as the total baryonic mass or the total dynamical mass. This is illustrated in Fig. 5.2

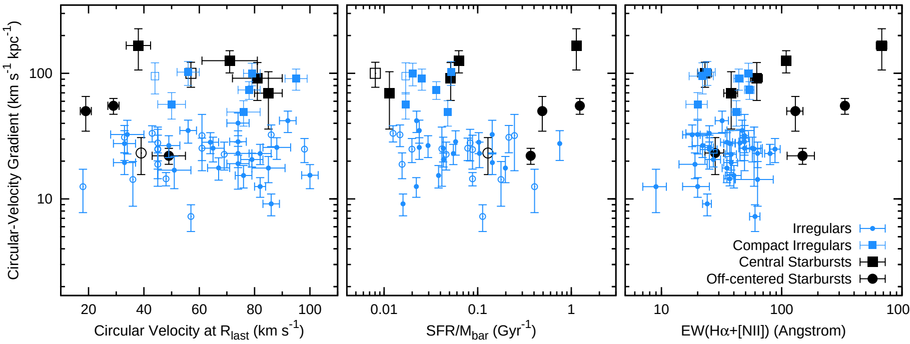

Figure 5.2 – *Left:* $V_{R_\mathrm{d}}/R_\mathrm{d}$ versus the circular velocity at the last measured point V_last. *Middle:* $V_{R_\mathrm{d}}/R_\mathrm{d}$ versus SFR/M_bar, where M_bar is estimated using the baryonic TF relation. *Right:* $V_{R_\mathrm{d}}/R_\mathrm{d}$ versus the Hα+[N II] equivalent width. Symbols are the same as in Fig. 5.1, except for the left and middle panels, where open symbols indicate galaxies with rotation curves that keep rising at V_last, thus their value of SFR/M_bar may be overestimated.

(left), where $V_{R_\mathrm{d}}/R_\mathrm{d}$ is plotted versus the circular-velocity at the last measured point V_last. Clearly, there is no correlation ($\rho_\mathrm{cc} \simeq 0.01$). Similarly, we found no correlation with the absolute magnitude M_R and with the dynamical mass (calculated at the last measured point). At every value of V_last (or M_R), one can find both high-surface-brightness (HSB) dwarfs with a steeply-rising rotation curve and low-surface-brightness (LSB) dwarfs with a slowly-rising rotation curve (cf. with Fig. 5.1, left). In particular, for a given V_last, BCDs typically have higher values of $V_{R_\mathrm{d}}/R_\mathrm{d}$ than the bulk of Irrs.

Fig. 5.1 clearly shows that BCDs are in the top-right part of the $V_{R_\mathrm{d}}/R_\mathrm{d} - \mu_0^i$ and $V_{R_\mathrm{d}}/R_\mathrm{d} - \overline{\Sigma}_\mathrm{H\,I}$ diagrams. This suggests that the starburst activity is closely linked to the inner shape of the potential well and to the central gas surface density. We can distinguish, however, between two types of BCDs: i) centrally-concentrated starbursts (NGC 1705, NGC 2915, NGC 4214, NGC 6789, and I Zw 18), and ii) diffuse and/or off-centered starbursts (NGC 2366, NGC 4068, UGC 4483, and I Zw 36). The former (black squares) have the highest values of $V_{R_\mathrm{d}}/R_\mathrm{d}$ and μ_0^i, whereas the latter (black dots) show moderate values of $V_{R_\mathrm{d}}/R_\mathrm{d}$ and μ_0^i. In particular, NGC 2366 and UGC 4483 are prototype "cometary" BCDs (e.g. Noeske et al. 2000), as the starburst region is located at the edge of an elongated LSB stellar body (see the Atlas in Chapter 4). I Zw 36 has an off-centered starburst region superimposed on an elliptical stellar body, and may be a "cometary-like" BCD observed close to face-on. Finally, NGC 4068 has several small star-forming regions spread over the entire stellar body. It is possible that BCDs with a diffuse/off-centered starburst are different from BCDs with a centrally-concentrated starburst in terms of their structure and dynamics. This may be related to different evolutionary histories and/or triggering mechanisms.

Several Irrs have circular-velocity gradients comparable to those of BCDs ($\gtrsim$ 45 km s^{-1} kpc^{-1}). These objects, shown by blue squares in Figs 5.1 and 5.2, are the following (the classification from de Vaucouleurs et al. 1991 is given): UGC 3711 (IBm), UGC 3966 (Im), UGC 5721 (SBd?), UGC 7232 (Im pec), UGC 7261 (SBdm), UGC 7690 (Im), and UGC 8490 (Sm). These galaxies have structural and dynamical properties more similar to BCDs than to typical Irrs. In particular, they have HSB exponential profiles with relatively-small scale-lengths ($\lesssim$1 kpc, see the right panel of Fig. 5.5) and strong concentrations of gas near the galaxy center (cf. Swaters & Balcells 2002). This suggests that either they are also starbursting dwarfs (and may be considered as BCDs) or they are progenitors/descendants of BCDs. Except for the barred galaxies UGC 3711 and UGC 7261, the surface brightness profiles of these Irrs do *not* show the central "light excess" that is typically observed in BCDs (cf. Swaters et al. 2002), thus it is likely that they are *not* experiencing a starburst at the present epoch. We will refer to them as compact Irrs. The study of the SFHs of these compact Irrs may be crucial to address their relation to BCDs.

5.4.2 Gravitational potential and starburst indicators

To clarify the relation between the gravitational potential and the star-formation, we plotted $V_{R_\mathrm{d}}/R_\mathrm{d}$ against several starburst indicators: the ratio SFR/M_bar (similar to sSFR=SFR/M_*), the equivalent width EW(Hα+[N II]), the SFR surface density Σ_SFR, and the gas depletion times t_local and t_global (see Sect. 5.3.3 for details). In the literature, there is no general agreement about which of these indicators best identifies a starburst galaxy.

The ratio SFR/M_bar quantifies the star-formation activity of a galaxy with respect to its baryonic mass (stars and atomic gas). This is comparable to SFR/M_*, which is often used for massive galaxies. We prefer to use SFR/M_bar for two reasons: i) we do not have a direct estimate of M_* for the Irrs, whereas we can estimate M_bar using the baryonic TF relation (see Sect. 5.3.3 for details), and ii) in some dwarf galaxies the atomic gas mass can be as high as the stellar mass, thus a LSB Irr that has been inefficiently forming stars during the Hubble time might have a relatively-high SFR/M_*-ratio but a low SFR/M_bar-ratio. The differences between SFR/M_bar and SFR/M_*, however, are typically within a factor of $\sim$2. Figure 5.2 (middle) shows that there is no correlation between $V_{R_\mathrm{d}}/R_\mathrm{d}$ and SFR/M_bar ($\rho_\mathrm{cc} \simeq -0.1$). Moreover, BCDs and Irrs can have similar values of SFR/M_bar, suggesting that this is not a good starburst indicator.

The EW(Hα) is thought to trace the stellar birthrate parameter b, defined as the ratio of the current SFR to the past, average SFR over the galaxy lifetime (e.g. Kennicutt 1998a). Lee et al. (2009) argued that an EW(Hα)$\gtrsim$ 100 Å corresponds to $b \gtrsim 2.5$ and, thus, indentifies a starburst. Fig. 5.2 (right) shows that there is no strong correlation between EW(Hα+[N II]) and $V_{R_\mathrm{d}}/R_\mathrm{d}$ ($\rho_\mathrm{cc} \simeq 0.3$). Most BCDs, as expected, have very high values of EW(Hα+[N II]), although some of them have EW(Hα+[N II])<100 Å. As pointed out by

McQuinn et al. (2010a), starbursts are events lasting for a few 100 Myr, whereas the Hα emission probes the star-formation activity over shorter timescales ($\lesssim$10 Myr), thus fluctuations in the SFH over a few Myr may explain why a EW(Hα) treshold misidentifies some BCDs.

The $\Sigma_{\rm SFR}$ normalizes the SFR by the area of the stellar body. Fig. 5.3 (left) shows that $V_{R_{\rm d}}/R_{\rm d}$ correlates with $\Sigma_{\rm SFR}$ ($\rho_{\rm cc} \simeq 0.8$). This suggests that there is a close link between the star-formation activity and the inner steepness of the potential well. A linear, error-weighted fit to the data returns

$$\log(V_{R_{\rm d}}/R_{\rm d}) = (0.36 \pm 0.04)\,\log(\Sigma_{\rm SFR}) + (2.6 \pm 0.1). \qquad (5.12)$$

This correlation is expected from Fig. 5.1 (right) and the Kennicutt-Schmidt (KS) law (e.g. Kennicutt 1998b). By combining Eq. 5.11 and Eq. 5.12, indeed, one can obtain a KS type of relation, that considers the atomic gas only and has a slope of $\sim$3. This is in line with the results of Roychowdhury et al. (2009), who investigated the KS law in 23 extremly-faint dwarf galaxies ($M_{\rm B} \simeq -13$ mag) and found a slope of $\sim$2.5 by considering atomic gas only and UV-based SFRs. As expected, starbursting dwarfs are in the top-right part of the $V_{R_{\rm d}}/R_{\rm d} - \Sigma_{\rm SFR}$ diagram. In BCDs, the starburst typically increases the SFR by a factor of $\sim$5 to $\sim$10 (e.g. McQuinn et al. 2010a). NGC 6789, which is the only *known* post-starburst galaxy in our sample (see McQuinn et al. 2010a and Sect. 5.5.2), shows a large horizontal deviation with respect to the main relation ($\gtrsim$1 dex). Intriguingly, compact Irrs also have high values of $\Sigma_{\rm SFR}$, but they systematically lie on the left side of the linear-fit by $\sim$0.5 to $\sim$1 dex, thus they are consistent with being progenitors/descendants of BCDs. However, the overall, large scatter on the $V_{R_{\rm d}}/R_{\rm d} - \Sigma_{\rm SFR}$ relation prevents us from reaching any firm conclusion about the nature of compact Irrs and their link with BCDs.

We point out that $V_{R_{\rm d}}/R_{\rm d} = 2\pi/\tau_{\rm orb}$, where $\tau_{\rm orb}$ is the orbital time on the solid-body portion of the rotation curve. Kennicutt (1998b) found that, for spiral galaxies and massive starbursts, $\Sigma_{\rm SFR}$ also correlates with $\Sigma_{\rm gas}/\tau_{\rm orb}$, where $\tau_{\rm orb}$ was calculated at the outer edge of the optical disk (presumably along the flat part of the rotation curve) and $\Sigma_{\rm gas}$ includes both atomic and molecular gas. This correlation may be interpreted as the effect of spiral arms triggering the star-formation (e.g. Kennicutt 1998b). Fig. 5.3 (right) shows that a similar correlation (with $\rho_{\rm cc} \simeq 0.9$) holds also for gas-rich dwarfs, in which the effect of density waves clearly cannot be important. Here $\tau_{\rm orb}$ is calculated on the solid-body portion of the rotation curve, while $\Sigma_{\rm gas}$ includes the atomic gas component only, since the molecular content of low-metallicity, dwarf galaxies is very uncertain (e.g. Taylor et al. 1998; Leroy et al. 2008). As discussed by Kennicutt (1998b), one might expect a linear relation of the form:

$$\Sigma_{\rm SFR} = \epsilon\, \Sigma_{\rm gas}/\tau_{\rm orb} \qquad (5.13)$$

where ϵ is the fraction of gas that is converted into stars during every orbit. For spiral galaxies and massive starbursts, Kennicutt (1998b) found that $\sim$10% of

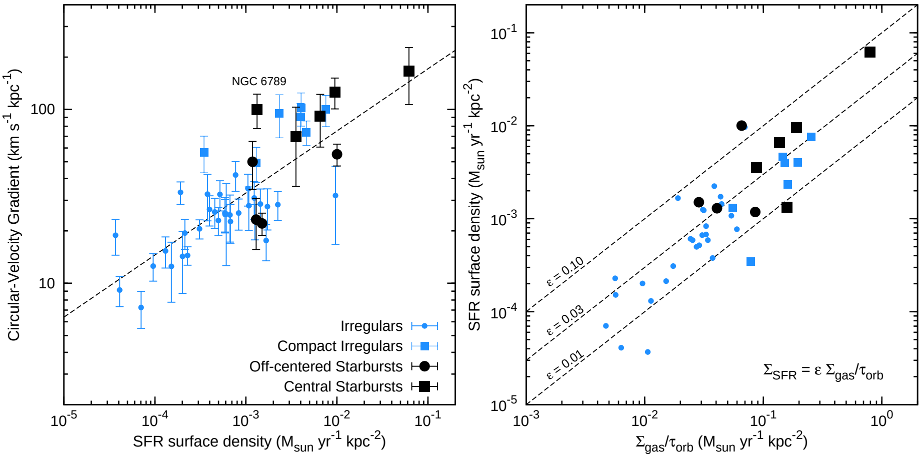

Figure 5.3 – *Left:* $V_{R_{\rm d}}/R_{\rm d}$ versus the SFR surface density $\Sigma_{\rm SFR}$. The dashed line shows a linear-fit to the data. The position of the post-starburst dwarf galaxy NGC 6789 is indicated. *Right:* $\Sigma_{\rm SFR}$ versus $\Sigma_{\rm gas}/\tau_{\rm orb}$, where $\Sigma_{\rm gas}$ considers the atomic gas only and $\tau_{\rm orb}$ is the orbital time on the solid-body portion of the rotation curve. The dashed lines show a linear relation for different value of ϵ. Symbols are the same as in Fig. 5.1.

the available gas (atomic plus molecular) is converted into stars during every orbit. The dashed lines in Fig. 5.3 (right) show fractions $\epsilon = 0.01$, 0.03, and 0.10. Most dwarf galaxies have $0.01 \lesssim \epsilon \lesssim 0.03$, but several BCDs seem to have $\gtrsim 0.03$, suggesting that they might be converting gas into stars more efficiently than other gas-rich dwarfs. However, metallicity and/or internal extinction may affect the relative values of $\Sigma_{\rm SFR}$ in different galaxies, thus it is unclear whether the differences in ϵ are real *or* due to the use of the same SFR calibration for all the galaxies, without considering the possible effects of internal extinction and metallicity.

Finally, $\tau_{\rm local}$ and $\tau_{\rm global}$ estimate the time that a galaxy will take to consume its gas reservoir, if it keeps forming stars at the current rate. $\tau_{\rm local}$ takes into account only the atomic gas within the stellar component, while $\tau_{\rm global}$ takes into account the total atomic gas. Since our SFRs may be slightly overestimated, the values of $\tau_{\rm local}$ and $\tau_{\rm global}$ may be underestimated by a factor of $\sim$2 (see Sect. 5.3.3). Several studies (e.g. van Zee 2001; Hunter & Elmegreen 2004) have shown that gas-rich dwarfs have long gas-depletion times (> 10 Gyrs) and, thus, could keep forming stars for several Hubble times. In Fig. 5.4 (left), we show that $V_{R_{\rm d}}/R_{\rm d}$ correlates with $\tau_{\rm local}$ ($\rho_{\rm cc} \simeq -0.8$), as expected from Figs. 5.1 (right) and 5.3 (left). BCDs and compact Irrs typically have $\tau_{\rm local} \lesssim 5$ Gyr. A linear, error-weighted fit to the data yields

$$\log(V_{R_{\rm d}}/R_{\rm d}) = (-0.43 \pm 0.06)\, \log(\tau_{\rm local}) + (1.87 \pm 0.06). \tag{5.14}$$

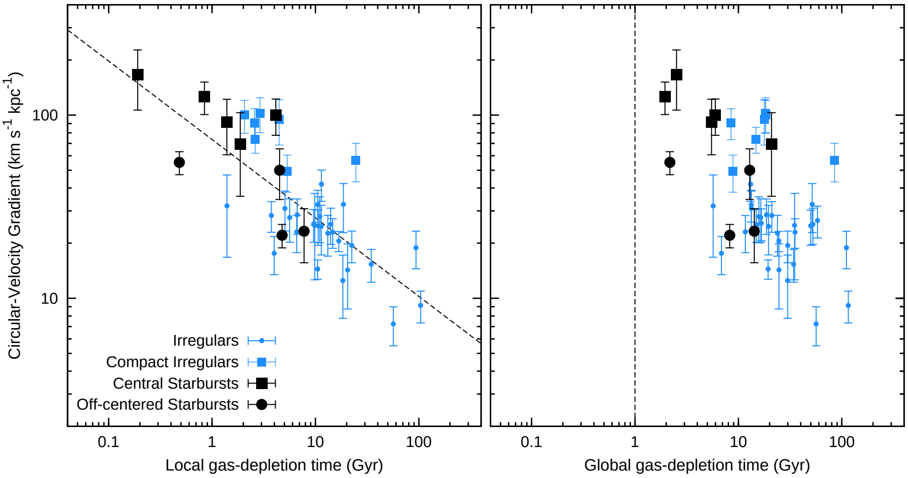

Figure 5.4 – *Left:* V_{R_d}/R_d versus the local gas-depletion time, that takes into account the atomic gas mass within the R_{opt}. The dashed line show a linear fit to the data. *Right:* V_{R_d}/R_d versus the total gas-depletion time, that takes into account the total atomic gas mass. The dashed line shows the maximum duration of a typical starburst (∼1 Gyr). Symbols are the same as in Fig. 5.1.

Figure 5.4 (right), instead, shows that the relation between V_{R_d}/R_d and τ_{global} is less well defined ($\rho_{cc} \simeq -0.6$). It also shows that τ_{global} is significantly larger than τ_{local}, implying that Irrs and BCDs have massive gas reservoirs outside the stellar component. For most BCDs, both τ_{local} and τ_{global} are larger than the typical durations of the burst (few 100 Myr), implying that they do not consume their entire gas reservoir during the current event of intense star-formation. Burst durations can be estimated using the SFHs derived by fitting the color-magnitude diagrams of the resolved stellar populations (e.g. McQuinn et al. 2010a). In particular, the sample of McQuinn et al. (2010a) includes five “fossil” starbursting dwarfs, that allows us to estimate the *total* duration of the burst. If one defines the burst duration as the period when $b > 2$, Fig. 2 of McQuinn et al. (2010b) shows that the longest burst duration is ∼850 Myr in UGC 9128. McQuinn et al. (2010b) report slightly higher values as they use a less conservative definition of “burst duration”. We assume a fiducial value of 1 Gyr as the maximum duration of a starburst; this is indicated in Fig. 5.4 by a verical dashed-line. All the BCDs in our sample have $\tau_{global} > 1$ Gyr, and most of them also have $\tau_{local} > 1$ Gyr.

5.4.3 Gas-poor dwarf galaxies

We now compare the structural and dynamical properties of gas-rich dwarfs with those of rotating Sphs in the Virgo cluster (van Zee et al. 2004a,b). The

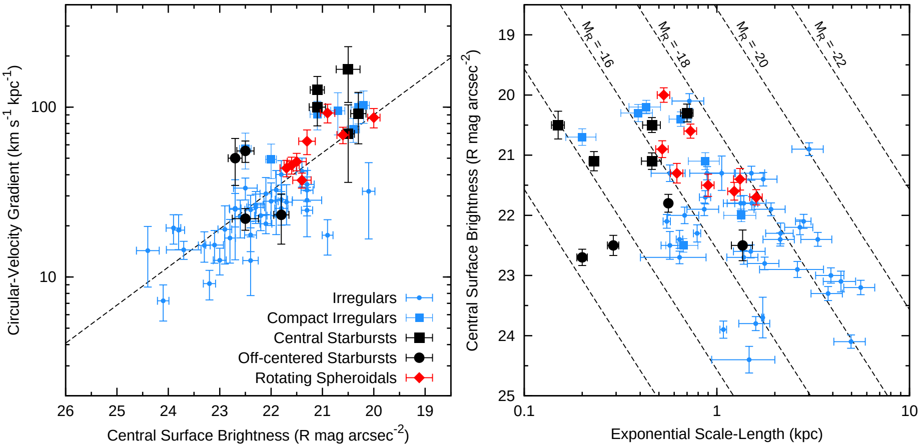

Figure 5.5 – *Left:* $V_{R_\mathrm{d}}/R_\mathrm{d}$ versus μ_0^i including rotating Sphs in the Virgo cluster (red diamonds). The other symbols are the same as in Fig. 5.1. The dashed line shows a linear fit to the Irr and BCD data (same as in Fig. 5.1). The stellar rotation velocities have been corrected for asymmetric drift (see Appendix 5.A). *Right*: R_d against μ_0^i. The dashed lines correspond to exponential profiles with a fixed total magnitude (-22, -20, -18, -16, -14, and -12 R mag).

stellar rotation velocities have been corrected for pressure-support as described in Appendix 5.A.

Figure 5.5 (left) shows that rotating Sphs follow the same correlation between $V_{R_\mathrm{d}}/R_\mathrm{d}$ and μ_0^i defined by Irrs and BCDs. Moreover, these rotating Sphs have values of $V_{R_\mathrm{d}}/R_\mathrm{d}$ and μ_0^i comparable with those of BCDs and compact Irrs. In Fig. 5.5 (right), we plot R_d against μ_0^i; the dashed lines correspond to exponential profiles with a fixed total magnitude. The rotating Sphs have total R-band magnitudes in the range $-16 \lesssim M_\mathrm{R} \lesssim -18$, comparable to the Irrs considered here. In general, for a given M_R, the values of μ_0^i and R_d of rotating Sphs are, respectively, higher and smaller than those of typical Irrs, but comparable with those of some BCDs and compact Irrs. Therefore, the structural and dynamical properties of rotating Sphs in the Virgo cluster appear similar to those of BCDs and compact Irrs in the field and nearby groups.

Since our sample of gas-poor dwarfs is relatively small, it is unclear whether rotating Sphs are necessarily more compact than typical Irrs, or whether this is the result of selection effects. It is clear, however, that a close link between the central dynamical mass density ($V_{R_\mathrm{d}}/R_\mathrm{d}$) and the stellar surface density (μ_0^i) is present in any kind of rotating galaxy (see also Lelli et al. 2013).

5.5 Discussion

5.5.1 The relation between gravitational potential, gas surface density, and starburst activity

In Sect. 5.3.1 we estimated the circular-velocity gradient $d_R V(0) \simeq V_{R_\mathrm{d}}/R_\mathrm{d}$ for a sample of 60 dwarf galaxies, including BCDs, Irrs, and Sphs. $V_{R_\mathrm{d}}/R_\mathrm{d}$ is a direct measure of the central dynamical mass density in a galaxy (including gas, stars, and dark matter). In Sect. 5.4.1 we showed that, for gas-rich dwarfs, $V_{R_\mathrm{d}}/R_\mathrm{d}$ correlates with i) the central surface brightness, ii) the mean H I surface density over the stellar body, and iii) the SFR surface density. Starbursting dwarfs are in the upper parts of these relations, as they have high H I surface densities, high central surface brightnesses, and high circular-velocity gradients, indicating that they have a high central dynamical mass density. This implies that the starburst activity is closely related to the inner steepness of the potential well and the gas surface density. The nature of this connection is unclear. There are, however, two likely possibilities: i) the progenitors of BCDs are unusually compact Irrs with a steep potential well, or ii) there is a mechanism that concentrates the mass (gas, stars, and dark matter) in typical Irrs, eventually causing a starburst. These possibilities are discussed in the following.

If the progenitors of BCDs are compact Irrs, the high circular-velocity gradient would imply high values of the critical surface-density threshold for gravitational instabilities Σ_crit (Toomre 1964; Kennicutt 1989) and make the gaseous disk relatively stable against large-scale perturbations. For a self-gravitating gaseous disk, Σ_crit is given by

$$\Sigma_\mathrm{crit} = \alpha \frac{\sigma_\mathrm{gas} \kappa}{\pi G} \tag{5.15}$$

where α is a dimensionless parameter (near unity) that accounts for the finite thickness of the disk (e.g. Martin & Kennicutt 2001), σ_gas is the gas velocity dispersion, and κ is the epicyclic frequency given by

$$\kappa = 1.41 \frac{V_\mathrm{circ}(R)}{R} \sqrt{1 + \frac{d \log V_\mathrm{circ}(R)}{d \log R}}. \tag{5.16}$$

The possible role of Σ_crit in BCDs has been discussed by Meurer et al. (1998) and van Zee et al. (2001), who argued that, in these compact galaxies, the gas could pile up in the center and reach high surface densities, while the star formation would be delayed until the critical surface-density treshold is reached, leading to a starburst. We note that this should strictly apply only to the inner regions of the galaxy ($R \lesssim 2R_\mathrm{d}$), where the shape of the rotation curve is close to a solid body and, thus, $\Sigma_\mathrm{crit} \propto V_{R_\mathrm{d}}/R_\mathrm{d}$ (assuming that σ_gas and α are nearly constant with radius). In the outer regions ($R \gtrsim 2R_\mathrm{d}$), instead, the rotation curve becomes flat and $\Sigma_\mathrm{crit} \propto 1/R$, hence the gaseous disk might be less stable. Thus, this picture does not require a "bursty" SFH for the whole galaxy, i.e. strong bursts separated by quiescent periods, as the star-formation may continue in the outer parts of the galaxy. Star-formation at large radii is actually observed in several Irrs and BCDs (e.g. Hunter & Elmegreen 2004).

Toomre's model for gravitational instabilities may also provide a simple explanation for the correlation between $V_{R_{\rm d}}/R_{\rm d}$ and $\overline{\Sigma}_{\rm H\,I}$ (Fig. 5.1, right). If $\Sigma_{\rm gas} \simeq \Sigma_{\rm crit} \propto V_{R_{\rm d}}/R_{\rm d}$ and the product $\alpha \times \sigma_{\rm gas}$ is approximately the same in every dwarf galaxy, we would expect the following relation:

$$\log\left(\frac{V_{R_{\rm d}}}{R_{\rm d}}\right) = \log(\Sigma_{\rm gas}) + \log\left(\frac{\pi G}{\alpha \sigma_{\rm gas}}\right). \tag{5.17}$$

Remarkably, the observed slope of the $V_{\rm R_d}/R_{\rm d} - \overline{\Sigma}_{\rm H\,I}$ relation is consistent with 1 within the uncertainties (see Eq. 5.11). Moreover, the value of the intersect (corrected for the presence of Helium) imply $\alpha \times \sigma_{\rm gas} = 3.6$ km s^{-1}, in close agreement with the value of $\sim$4 km s^{-1} found by Kennicutt (1989) and Martin & Kennicutt (2001) in the outer regions of spiral galaxies. Note that Eq. 5.15 and Eq. 5.17 are valid in the case of a self-graviting gaseous disk. If one considers also the gravitational effect of stars, the condition for the stability of the two-components disk is more complex (e.g. Rafikov 2001), and it is unclear whether the linear relation in Fig. 5.1 (right) may be simply explained.

There are several mechanisms that can cause a concentration of mass in a galaxy, both internal (bar-like torques) and/or external (interactions/mergers). First, we discuss internal mechanisms. BCDs and compact Irrs are not necessarily barred, thus a bar-driven inflow seems an unlikely general mechanisms. However, Hunter & Elmegreen (2004) speculated that dwarf galaxies may have bars made of dark matter, while Bekki & Freeman (2002) argued that rotating, triaxial dark-matter haloes can exert large-scale torques and lead to mass inflow. Elmegreen et al. (2012) proposed that massive clumps of gas and young stars can exchange angular momentum with halo stars and dark matter particles and, thus, may spiral inward to the galaxy center, leading to a central starburst. This scenario would imply an evolutionary trend from BCDs with an off-centered starbursts (e.g. NGC 2366 and I Zw 36) to BCDs with a centrally-concentrated starburst (e.g. NGC 1705 and NGC 4214). Simulations of high-redshift galaxies suggest that the clump-instability creates a central mass concentration similar to a bulge, that is photometrically distinct from the underlying exponential disk (e.g. Immeli et al. 2004; Bournaud et al. 2007). The compact Irrs identified in Sec. 5.4.1, instead, have surface brightness profiles described by a single HSB exponential (with the exception of the barred galaxies UGC 3711 and UGC 7261; cf. Swaters & Balcells 2002). BCDs often show surface brightness profiles with an inner light excess, but these light enhancements typically have very blue colors and do not appear to trace the stellar mass (e.g. Papaderos et al. 1996).

Regarding external mechanims, it is well established that galaxy interactions and mergers can cause gas inflow and lead to a central starburst (e.g. Barnes

& Hernquist 1996; Bekki 2008). Moreover, dwarf galaxies are thought to be relatively fragile systems and external perturbations may significantly change their mass distribution, possibly leading to an overall contraction of the stellar and gaseous disks (e.g. Hunter & Elmegreen 2004). About half of the BCDs in our sample have disturbed and asymmetric H I morphologies in their outer parts, suggesting either a recent interaction/merger between gas-rich dwarfs (see e.g. I Zw 18 in Lelli et al. 2012a) or gas accretion from the environment (e.g. Kereš et al. 2005; Dekel & Birnboim 2006). Disturbed H I morphologies have been found also in other studies of BCDs (e.g. López-Sánchez et al. 2010; Ashley et al. 2013) and several interacting BCDs are known (e.g. Cox et al. 2001; Ekta et al. 2006, 2009). Thus, the hypothesis that interactions/mergers cause the central concentration of mass (gas, stars, and/or dark matter) and trigger the starburst is in overall agreement with the observations.

5.5.2 BCDs and the evolution of dwarf galaxies

In the following, we discuss the possible evolutionary links between BCDs, Irrs, and Sphs. The emerging picture is that a BCD in isolation most likely evolves into a compact Irr, but environmental processes (such as ram-pressure stripping) may transform compact Irrs and BCDs into rotating Sphs.

The link between BCDs and compact Irrs

In Sect. 5.4.1 we pointed out that the global gas-depletion times of BCDs are much larger than the typical durations of a starburst (<1 Gyr). This implies that BCDs generally do not consume their entire gas reservoir. Moreover, both optical and X-rays observations suggest that BCDs do not expell a large quantity of gas out of their potential well (see also Chapter 4). Observations of the Na D absorption doublet have shown that ouflows are common in starbursting dwarfs, but the velocities of the outflowing gas do *not* clearly exceed the galaxy escape velocity (Schwartz & Martin 2004). Similarly, studies of the Hα kinematics have found that the warm gas is usually gravitationally-bound to the galaxy (e.g. Martin 1996, 1998; van Eymeren et al. 2009b,a, 2010). X-ray studies have revealed that some BCDs have diffuse coronae of hot gas at $T \simeq 10^6$ K (Ott et al. 2005a,b), which are presumably associated with outflows but have very low masses, only ∼1% of the H I masses. Thus, a BCD *in isolation* most likely evolves into another gas-rich dwarf as the starburst fades.

In Sect. 5.4.1 we also identified several compact Irrs that have structural and dynamical properties similar to BCDs. It is clear that, unless a redistribution of mass takes place, the descendants of BCDs must be compact Irrs. A strong redistribution of mass seems unlikely for two reasons: i) in dwarf galaxies there are no *known* internal mechanisms that are able to redistribute stars and dark matter, such as radial migrations due to bars and density waves (e.g. Minchev et al. 2011); and ii) stellar feedback seems unable to expell a large quantity of gas from the potential well and, thus, cause a significant expansion of the stellar and dark matter components. In particular, Papaderos et al. (1996) and Gil de Paz & Madore (2005) showed that the scale-lengths of the old stellar component of BCDs should, on average, increase by a factor of ∼2 to be consistent with those of typical Irrs and Sphs. Papaderos et al. (1996) proposed a simple, spherically-symmetric model to quantify the effect of ouflows on the evolution of the stellar body of an isolated BCD; their equations 12 and 13 can be written as

$$\frac{R_{\rm d}^{\rm i}}{R_{\rm d}^{\rm f}} = 1 - \frac{M_{\rm out}}{M_{\rm bar}^{\rm i}} f_{\rm bar}^{\rm i} \tag{5.18}$$

where $R_{\rm d}^{\rm i}$ and $R_{\rm d}^{\rm f}$ are, respectively, the scale-lengths in the initial (starburst) and final (post-starburst) stages of the system, $M_{\rm out}$ is the gas mass that is ejected, $M_{\rm bar}^{i} = M_{*} + M_{\rm gas}$ is the baryonic mass in the initial stage, and $f_{\rm bar}^{\rm i} = M_{\rm bar}^{\rm i}/M_{\rm dyn}^{\rm i}$ is the initial baryonic fraction within the stellar body. In Chapter 4, we showed that BCDs have, on average, $f_{\rm bar} \simeq 0.3$ to 0.5, depending on the assumptions on the IMF and on the molecular gas content. In order to have $R_{\rm d}^{\rm i}/R_{\rm d}^{\rm f} = 1/2$, one would need unphysical values of $M_{\rm out}/M_{\rm bar}^{\rm i} \simeq 1$ to 1.7, that would leave no baryons in the potential well. Thus, even if outflows would expell a significant quantity of gas, they could not easily explain the differences in the scale-lengths of BCDs and typical Irrs/Sphs.

In this evolutionary context, the BCD NGC 6789 deserves special attention. NGC 6789 resides in the Local Void and is extremely isolated, as the nearest massive galaxy (NGC 6946) is at a projected distance of 2.5 Mpc (Drozdovsky et al. 2001). The SFHs from McQuinn et al. (2010a) and García-Benito & Pérez-Montero (2012) show that the starburst ended about ∼500 Myr ago and the galaxy is now forming stars at a lower rate. Thus, NGC 6789 is a post-starburst dwarf galaxy. The system still has a considerable gas reservoir ($\sim 2\times 10^{7}$ M$_{\odot}$) and the gas depletion time is long (∼6 Gyr). The rotation curve rises steeply in the inner parts, indicating that there is a strong central concentration of mass. Thus, NGC 6789 did not consume its entire gas reservoir during the starburst and did not experience a strong redistribution of mass in the last ∼500 Myr, in agreement with our previous reasoning.

The link between BCDs and rotating Sphs

In Sect. 5.4.3, we showed that rotating Sphs in the Virgo cluster have central dynamical mass densities similar to those of BCDs and compact Irrs. It is likely, therefore, that rotating Sphs are the descendants of BCDs and compact Irrs, providing that some mechanism removes the gas from the galaxy. As we already pointed out, supernova feedback seems unable to entirely expell the ISM of a BCD, thus the best candidate is ram-pressure stripping due to either the hot intra-cluster medium (e.g. Kormendy & Bender 2012) or the hot coronae that are thought to surround massive galaxies (e.g. Gatto et al. 2013).

The rotating Sphs in our sample, however, are still pressure-supported in the inner regions (with $v_{\rm rot}/\sigma$ between $\sim$0.3 to $\sim$1), whereas the *gaseous disks* of BCDs and Irrs are rotation-supported (with $v_{\rm rot}/\sigma > 1$). In particular, one may expect that the newly-formed stars retain the angular momentum of the H I disk, which is the site of the recent star-formation. Thus, an additional mechanism that heats the stellar disk of a BCD/compact Irr may be required for a morphological transformation into a rotating Sph. Possible mechanisms are galaxy harassment by a galaxy cluster (e.g. Moore et al. 1998) or tidal stirring by a nearby massive companion (e.g. Mayer et al. 2006). We warn, however, that the comparison between different kinematical tracers (as stars and H I) may be misleading. Leaman et al. (2012) studied the stellar kinematics of the Local Group irregular WLM and found that its stellar disk has $v_{\rm rot}/\sigma \sim 1$, whereas the H I disk has $v_{\rm rot}/\sigma \sim 7$. Thus, the stellar and H I kinematics in a dwarf galaxy may be remarkably different, and the stellar component of an Irr may be very similar to that of a Sph. In this case, the evolution from a BCD/compact Irr to a rotating Sph would just require gas removal, given that the current starburst typically creates only a small fraction of the total stellar mass ($\sim$10%, e.g. McQuinn et al. 2010b) and, thus, the newly-formed stars cannot strongly affect the overall stellar kinematics.

The evolutionary sequence BCDs → compact Irrs → rotating Sphs may solve some long-standing issues about the direct transformation of Irrs into *bright* Sphs: i) Irrs are expected to fade after the cessation of the star-formation and this would result in central surface brightnesses that are significantly lower than those of the brightest Sphs in galaxy clusters (Bothun et al. 1986; Davies & Phillipps 1988), and ii) most bright Sphs show central nuclei whereas Irrs do not (e.g. Côté et al. 2006; Lisker et al. 2007). In fact, regardless of the details of the triggering mechanism, the occurrence of a starburst in an Irr should necessarily i) create a central concentration of mass and increase the central surface brightness, and might possibly ii) form a central nucleus by the inspiralling and merging of star clusters (Gnedin et al. 2013), which are often found in BCDs (e.g. Annibali et al. 2009, 2011). In particular, the nuclei of Sphs are generally bluer than the overall stellar body (e.g. Lotz et al. 2004), suggesting that they contain younger stellar populations than the rest of the galaxy. Moreover, several Sphs in the Virgo cluster show central star-formation and/or disk features (e.g. Lisker et al. 2006, 2007), further hinting at a possible link with BCDs and compact Irrs.

Finally, we point out that the rotating Sphs considered here have relatively-high luminosities ($-16 \lesssim M_{\rm R} \lesssim -18$ mag) and, thus, are at the top end of the $M - \mu_0$ relation (e.g. Kormendy et al. 2009). It is unclear whether Sphs with lower luminosities and surface brightnesses, as those in the Local Group, also show some ordered rotation (see e.g. Tolstoy et al. 2009) and what their location is in the $V_{\rm R_d}/R_{\rm d} - \mu_0$ diagram. Thus, the evolutionary scenario outlined above refers *only* to the brightest Sphs found in galaxy clusters. Typical LSB Irrs might evolve into LSB Sphs without going through a starbursting phase (e.g. Weisz et al. 2011).

5.6 Conclusions

We studied the structure and evolution of dwarf galaxies using a new dynamical quantity: the circular-velocity gradient $d_R V(0)$. This provides a direct measure of the inner steepness of the potential well of a galaxy and, thus, of its central dynamical mass density (including gas, stars, and dark matter). For bulgeless, low-mass galaxies, $d_R V(0)$ can be simply estimated as $V_{R_\mathrm{d}}/R_\mathrm{d}$, where R_d is the exponential scale-length of the stellar body. We constructed a sample of 60 low-mass galaxies (including starbursting dwarfs, irregulars, and spheroidals), considering objects with high-quality H I and stellar rotation curves from the literature. Our results can be summarized as follows.

1. For gas-rich dwarfs (Irrs and BCDs), $V_{R_\mathrm{d}}/R_\mathrm{d}$ correlates with i) the central surface brightness μ_0^i; ii) the mean H I surface density over the stellar body; and iii) the SFR surface density.

2. Starbursting dwarfs (BCDs) are different from typical Irrs. BCDs have high central surface brightnesses, high H I surface densities, and high circular-velocity gradients, implying that they have a strong central concentration of dynamical mass (luminous and/or dark). This suggests that the starburst is closely linked to the inner shape of the gravitational potential and the gas density.

3. We identified several compact Irrs that have values of μ_0^i, R_d, and $V_{R_\mathrm{d}}/R_\mathrm{d}$ similar to those of BCDs. Compact Irrs are the best candidates to be the progenitors/descendants of BCDs.

4. Rotating Sphs in the Virgo cluster follow the same correlation between $V_{R_\mathrm{d}}/R_\mathrm{d}$ and μ_0^i determined by Irrs and BCDs. The Sphs in our sample have values of $V_{R_\mathrm{d}}/R_\mathrm{d}$ similar to those of BCDs and compact Irrs. This suggests that BCDs and compact Irrs may evolve into rotating Sphs, provided that some external mechanism removes the entire ISM.

5. Similarly to spiral galaxies, the star-formation activity in dwarfs can be described by a law of the form $\Sigma_\mathrm{SFR} = \epsilon \, \Sigma_\mathrm{gas}/\tau_\mathrm{orb}$, where Σ_gas considers the atomic gas only, τ_orb is the orbital time on the solid-body portion of the rotation curve, and the fraction ϵ of atomic gas converted into stars during every orbit is $\sim 2\%$.

Acknowledgements

We are grateful to Renzo Sancisi for sharing insights and ideas that fueled this investigation. We also thank Eline Tolstoy for stimulating discussions. FL acknowledges the Ubbo Emmius bursary program of the University of Groningen and the Leids Kerkhoven-Bosscha Fund. FF aknowledges financial support from PRIN MIUR 2010-2011, project "The Chemical and Dynamical Evolution of the Milky Way and Local Group Galaxies", prot. 2010LY5N2T.

Appendix 5.A Asymmetric-drift correction

To calculate the asymmetric-drift correction, we start from equation (4-33) of Binney & Tremaine (1987), which describes a stationary, axisymmetric stellar system embedded in a gravitational potential $\Phi(R, z)$:

$$V_{\rm circ}^2 = \overline{v_\phi}^2 - \sigma_{\rm R}^2 \left[\frac{\partial \ln \rho}{\partial \ln R} + \frac{\partial \ln \sigma_{\rm R}^2}{\partial \ln R} + 1 - \frac{\sigma_\phi^2}{\sigma_{\rm R}^2} + \frac{R}{\sigma_{\rm R}^2} \frac{\partial (\overline{v_{\rm R} v_z})}{\partial z} \right], \tag{5.A.1}$$

where $v_{\rm R}$, v_z, and v_ϕ are the components (in cylindrical coordinates) of the velocity of a star, ρ is the stellar density, $\sigma_{\rm R}^2 = \overline{v_{\rm R}^2}$, $\sigma_{\rm z}^2 = \overline{v_{\rm z}^2}$, $\sigma_\phi^2 = \overline{v_\phi^2} - \overline{v_\phi}^2$, and $V_{\rm circ} = \sqrt{R(\partial\Phi/\partial R)}$. The observed stellar rotation curve $v_{\rm rot}$ provides $\overline{v_\phi}$. Note that equation 5.A.1 does *not* require that the velocity dispersion is smaller than the rotation velocity. Following Weijmans et al. (2008), we write

$$\overline{v_{\rm R} v_z} = \kappa(\sigma_{\rm R}^2 - \sigma_z^2) \frac{z/R}{1 - (z/R)^2} \qquad 0 \leq \kappa \leq 1, \tag{5.A.2}$$

where $\kappa = 0$ and $\kappa = 1$ correspond, respectively, to the extreme cases of a velocity ellipsoid aligned with the cylindrical (R, z, ϕ) and spherical (r, θ, ϕ) coordinate systems. Using higher-order velocity-moments of the collisionless Boltzmann equation, Weijmans et al. (2008) obtained the following expressions (see their Appendix A):

$$\frac{\sigma_\phi^2}{\sigma_{\rm R}^2} = \frac{1}{2} \left[1 + \alpha_{\rm R} + \kappa \frac{1 - \sigma_z^2/\sigma_{\rm R}^2}{1 - (z/R)^2} \alpha_z - \frac{\overline{(v_\phi - \overline{v_\phi})^3}}{\sigma_{\rm R}^2 \overline{v_\phi}} \right] \tag{5.A.3}$$

and

$$\frac{\sigma_\phi^2}{\sigma_z^2} = \frac{\kappa z^2 (1 + \alpha_{\rm R})}{\kappa z^2 (1 + \alpha_{\rm R}) - \alpha_z (R^2 - z^2)}, \tag{5.A.4}$$

where

$$\alpha_{\rm R} = \frac{\partial \ln \overline{v_\phi}}{\partial \ln R}, \quad \text{and} \quad \alpha_z = \frac{\partial \ln \overline{v_\phi}}{\partial \ln z}. \tag{5.A.5}$$

The last term of equation 5.A.3 vanishes if the velocity ellipsoid is symmetric around $\overline{v_\phi}$. Since we want to estimate $V_{\rm circ}$ at $R \simeq R_{\rm d}$, this higher-order term can be safely ignored, as $\sigma_{\rm R}^2 \simeq \sigma_{\rm obs}^2 > \overline{v_\phi}^2$ in the inner galaxy regions.

We now assume that the galaxy is in cylindrical rotation, i.e. $v_{\rm rot} = \overline{v_\phi}(R)$. Observationally, it is difficult to obtain information on the rotation velocities above the galaxy plane. A negative velocity gradient in the vertical direction, however, would produce an observable feature: asymmetric line profiles with a tail toward the systemic velocity. This means that a Gauss-Hermite polynomial-fit to the line profiles should give high values of the h_3 term. This effect is observed, for example, in the lagging H I haloes of spiral galaxies (e.g. Fraternali et al. 2002). The stellar, absorption-line profiles of gas-poor dwarfs, instead, are quite symmetric and have $|h_3| \lesssim 0.1$ (Halliday et al. 2001; Spolaor et al. 2010; Howley et al. 2013), implying that any vertical velocity gradient is relatively small. It is reasonable, therefore, to assume cilindrical rotation such that $\alpha_z = 0$. Thus, Eq. 5.A.4 gives $\sigma_\phi = \sigma_z$.

Since we are interested in the inner circular-velocity gradient, we also assume that the galaxy is in solid-body rotation, i.e. $\overline{v_\phi}(R) = A \times R$. All the Sphs in our sample, indeed, show nearly solid-body rotation curves out to the last measured point (cf. van Zee et al. 2004b) and thus $\alpha_R = 1$. Consequently, Eq. 5.A.3 gives $\sigma_\phi = \sigma_{\rm R}$ (neglecting the higher-order term). Therefore, using observationally-motivated assumptions, we find that the Sphs in our sample can be approximated as isotropic rotators with $\sigma_{\rm R} = \sigma_z = \sigma_\phi = \sigma_{\rm obs}$.

Finally, we assume that the scale-height of the galaxy is constant with radius. Thus, we have $\partial \ln \rho / \partial \ln R = \partial \ln \Sigma / \partial \ln R$, where Σ is the surface density profile (traced by the surface brightness profile). Assuming a Sersic profile (Sérsic 1963), the asymmetric-drift-corrected circular velocity is given by

$$V_{\rm circ}^2 = v_{\rm rot}^2 + \sigma_{\rm obs}^2 \left[\frac{b_n}{n} \left(\frac{R}{R_{\rm eff}} \right)^{1/n} - 2 \frac{\partial \ln \sigma_{\rm obs}}{\partial \ln R} \right], \tag{5.A.6}$$

where $R_{\rm eff}$ is the effective radius, n is the Sersic index, and b_n is a constant that depends on n (see Ciotti 1991; Ciotti & Bertin 1999).

For rotating Sphs, the surface brightness profile can be fitted by an exponential-law, thus $n = 1$ and $b_1 = 1.678$. We also assume that $\sigma_{\rm obs}$ is constant with radius, as the observations generally provide only the mean value $\overline{\sigma}_{\rm obs}$. Therefore, Eq. 5.A.6 simplifies to $V_{\rm circ}^2 = v_{\rm rot}^2 + \overline{\sigma}_{\rm obs}^2 (R/R_{\rm d})$, where $R_{\rm d} = 1.678 R_{\rm eff}$ is the exponential scale-length. In this case, the error $\delta_{V/R}$ on $V_{\rm R_d}/R_{\rm d}$ is given by

$$\begin{aligned} \delta_{V/R}^2 = \Bigg\{ & \left[\frac{v_{\rm rot}}{V_{\rm circ}} \frac{\delta_{v_{\rm l.o.s.}}}{R \sin(i)} \right]^2 + \left[\frac{v_{\rm rot}^2}{V_{\rm circ} R} \frac{\delta_i}{\tan(i)} \right]^2 \\ & + \left[\frac{\overline{\sigma}_{\rm obs}}{V_{\rm circ}} \frac{\delta_{\overline{\sigma}_{\rm obs}}}{R_{\rm d}} \right]^2 + \left[\frac{V_{\rm circ}}{R} \frac{\delta_D}{D} \right]^2 \Bigg\}_{R=R_{\rm d}}, \end{aligned} \tag{5.A.7}$$

where D and i are, respectively, the galaxy distance and inclination (cf. with Eq. 5.3).

Appendix 5.B Tables

Tables 5.B.1 and 5.B.3 - Structural and dynamical properties of gas-rich dwarfs (BCDs and Irrs)

Column (1) gives the galaxy name.
Column (2), (3), (4) give the assumed distance, the distance indicator, and the corresponding reference.
Column (5), (6), (7), and (8) give the R-band absolute magnitude $M_{\rm R}$, the central R-band surface brightness μ_0^i (corrected for inclination), the scale-length $R_{\rm d}$, and the reference for the surface photometry. The structural parameters were derived from an exponential fit to the outer parts of the surface brightness profiles. All the quantities have been corrected for Galactic extinction, but not for internal extiction.
Column (9) gives the galaxy inclination, derived by fitting a tilted-ring model to the H I velocity field and/or by building 3D model-cubes.
Column (10), (11), (12), and (13) give the circular velocity $V_{R_{\rm d}}$ at $R_{\rm d}$, the circular velocity $V_{\rm last}$ at the last measured point, the radius at $V_{\rm last}$, and the reference for the H I rotation curves. Values of $V_{\rm last}$ in *italics* indicate rotation curves that do not reach the flat part.
Column (15) gives the circular-velocity gradient $V_{R_{\rm d}}/R_{\rm d}$.

Tables 5.B.2 and 5.B.4 - Gas and star formation properties of gas-rich dwarfs (BCDs and Irrs)

Column (1) gives the galaxy name.
Column (2) and (3) give the gas metallicity and the respective references. Values in *italics* indicate abundances derived using “strong-line” calibrations; we assigned to them a conservative error of 0.2 (cf. Berg et al. 2012). All the other abundances have been derived using the T_e-method.
Column (4), (5), and (6) give the H I mass, the mean H I surface density within $R_{\rm opt} = 3.2 R_{\rm d}$ (corrected for inclination), and the reference for the H I observations.
Column (7), (8), and (9) give the Hα+[N II] equivalent width, the Hα star formation rate (SFR), and the reference for the Hα observations. SFRs have been calculated using the Kennicutt (1998a) calibration and have not been corrected for internal extinction.
Column (10) and (11) give the ratio SFR/$M_{\rm bar}$ and the SFR surface density ($\Sigma_{\rm SFR} = {\rm SFR}/\pi R^2_{\rm opt}$). $M_{\rm bar}$ has been estimated using the baryonic Tully-Fisher relation as calibrated by McGaugh (2012) with an accuracy of ∼10%. Values of SFR/$M_{\rm bar}$ in *italics* indicate galaxies with rotation curves that do not reach the flat part, thus they may be slightly underestimated.
Column (12) and (13) give the global and local gas depletion times $\tau_{\rm global}$ and

$\tau_{\rm local}$. $\tau_{\rm global}$ considers the total atomic gas mass of the galaxy, whereas $\tau_{\rm local}$ considers the atomic gas mass within $R_{\rm opt}$.

Table 5.B.5 - Structural and dynamical properties of gas-poor dwarfs (Sphs)

Column (1) gives the galaxy name.
Column (2), (3), (4), (5), and (6) give the R-band absolute magnitude, the inclination i, the central surface brightness (corrected for i), the scale-length, and the reference for the surface photometry. The inclination was estimated from the observed ellipticities using Eq. 5.6 with $q_0 = 0.35$. The structural parameters were derived from an exponential fit to the outer parts of the surface brightness profiles. All the quantities have been corrected for Galactic extinction, but not for internal extinction.
Column (7), (8), (9), (10), and (11) give the rotation velocity at $R_{\rm d}$, the rotation velocity $v_{\rm last}$ at the last measured point, the radius at $v_{\rm last}$, the mean velocity dispersion, and the reference for the stellar spectroscopy. All rotation velocities have been corrected for inclination.
Column (12), (13) and (14) give the circular velocity at $R_{\rm d}$, the circular velocity at $R_{\rm last}$, and the circular-velocity gradient. All the circular velocities have been corrected for asymmetric-drift (see Appendix 5.A).

Table 5.B.1 – Sample of starbursting dwarfs. Structural and dynamical properties. References: (a) Tosi et al. (2001); (b) Tolstoy et al. (1995); (c) Karachentsev et al. (2003); (d) Jacobs et al. (2009); (e) Drozdovsky et al. (2001); (f) Izotov & Thuan (2002); (g) Aloisi et al. (2007); (h) Schulte-Ladbeck et al. (2001); (i) Aloisi et al. (2005); (j) Chapter 4; (k) Swaters & Balcells (2002); (l) Meurer et al. (1994); (m) Papaderos et al. (2002); (n) Elson et al. (2010); (o) Lelli et al. (2012b); (p) Lelli et al. (2012a).

Name (1)	Dist (Mpc) (2)	Method (3)	Ref. (4)	$M_{\rm R}$ (mag) (5)	$\mu^{i}_{0,R}$ (mag/$''^2$) (6)	$R_{\rm d}$ (kpc) (7)	Ref. (8)	i ($^\circ$) (9)	$V_{R_{\rm d}}$ (km/s) (10)	$V_{\rm last}$ (km/s) (11)	$R_{\rm last}$ (kpc) (12)	Ref. (13)	$V_{R_{\rm d}}/R_{\rm d}$ (km/s/kpc) (14)
NGC 1705$^{\alpha}$	5.1±0.6	TRGB	a	-16.3±0.2	21.1±0.1	0.46	j	45±5	58±8	71±10	5.7	j	126±25
NGC 2366	3.2±0.4	Ceph	b	-16.6±0.3	22.5±0.2	1.36	k	68±5	30±2	49±6	5.9	j	22±3
NGC 2915$^{\beta}$	3.8±0.4	TRGB	c	-15.9±0.2	20.5±0.1	0.46	l	52±3	32±15	85±5	9.3	n	70±33
NGC 4068	4.3±0.1	TRGB	d	-15.7±0.1	21.8±0.1	0.56	k	44±6	13±4	*39±5*	2.3	j	23±8
NGC 4214$^{\alpha}$	2.7±0.2	TRGB	d	-17.8±0.2	20.3±0.1	0.70	k	30±10	64±8	81±9	4.8	j	91±31
NGC 6789	3.6±0.2	TRGB	e	-15.1±0.1	21.1±0.2	0.23	j	43±7	23±4	*57±9*	0.7	j	100±22
UGC 4483	3.2±0.2	TRGB	f	-13.0±0.1	22.7±0.1	0.20	j	58±3	10±3	19±2	1.2	o	50±15
I Zw 18$^{\gamma}$	18.2±1.4	TRGB	g	-15.0±0.2	20.5±0.2	0.15	m	70±4	25±10	38±4	0.8	p	167±60
I Zw 36	5.9±0.5	TRGB	h	-14.9±0.1	22.5±0.2	0.29	j	67±3	16±2	29±2	1.1	j	55±8

Notes. $^{(\alpha)}$ The H I disk is warped, the inclination is given for $R \simeq R_{\rm d}$.
$^{(\beta)}$ We adopted the rotation curve derived by Elson et al. (2010) assuming a constant inclination of 52°.
$^{(\gamma)}$ The optical parameters have been derived by Papaderos et al. (2002) after subtracting the Hα emission.

Table 5.B.2 – Sample of starbursting dwarfs. Gas and star-formation properties. References: (a) Berg et al. (2012); (b) Croxall et al. (2009); (c) Izotov & Thuan (1999); (d) Chapter 4; (e) Elson et al. (2010); (f) Kennicutt et al. (2008); (g) Gil de Paz et al. (2003).

Name (1)	log(O/H) +12 (2)	Ref. (3)	$M_{\rm H\,I}$ ($10^8 M_\odot$) (4)	$\overline{\Sigma}_{\rm H\,I}$ ($M_\odot$/pc^2) (5)	Ref. (6)	EW(Hα) (Å) (7)	SFR ($M_\odot$/yr) (8)	Ref. (9)	SFR/$M_{\rm bar}$ (Gyr^{-1}) (10)	log($\Sigma_{\rm SFR}$) ($M_\odot$/yr/kpc^2) (11)	$\tau_{\rm global}$ (Gyr) (12)	$\tau_{\rm local}$ (Gyr) (13)
NGC 1705	8.21±0.05	a	1.1±0.3	7.0±0.9	d	109±7	0.075	f	0.063	-1.96	1.9	0.8
NGC 2366	7.91±0.05	b	6.2±1.7	6.0±1.4	d	149±38	0.100	f	0.369	-2.77	8.2	4.7
NGC 2915	8.27±0.20	a	4.4±1.0	5.8±0.7	e	38±5	0.028	f	0.011	-2.39	20.9	1.9
NGC 4068	...	...	1.5±0.2	8.1±1.1	d	28±5	0.014	f	*0.129*	-2.89	14.2	8.3
NGC 4214	8.22±0.05	a	4.3±0.8	6.9±1.0	d	62±7	0.104	f	0.051	-2.18	5.5	1.4
NGC 6789	...	...	0.18±0.03	7.3±1.1	d	23±3	0.004	f	*0.008*	-2.63	6.0	4.1
UGC 4483	7.56±0.03	b	0.29±0.05	7.9±1.0	d	130±20	0.003	f	0.490	-2.63	12.9	4.5
I Zw 18	7.18±0.01	c	2.1±0.4	22.0±4.8	d	679±68	0.111	g	1.133	-0.81	2.5	0.2
I Zw 36	7.77±0.01	c	0.7±0.1	5.5±0.9	d	335±17	0.041	f	1.233	-1.82	2.3	0.5

Table 5.B.3 – Sample of irregulars. Structural and dynamical properties. References: (a) Tully (1988); (b) Tully et al. (2009); (c) Hoessel et al. (1998); (d) Thim et al. (2004); (e) Jacobs et al. (2009); (f) Drozdovsky & Karachentsev (2000); (g) Bono et al. (2010); (h) Swaters & Balcells (2002); (i) Tully et al. (1996); (j) Hunter & Elmegreen (2006); (k) Swaters et al. (2009); (l) Verheijen & Sancisi (2001); (m) Broeils (1992); (n) Kepley et al. (2007); (o) Weldrake et al. (2003).

Name (1)	Dist (Mpc) (2)	Method (3)	Ref. (4)	M_R (mag) (5)	$\mu_{0,R}^{i}$ (mag/$''^2$) (6)	R_d (kpc) (7)	Ref. (8)	i (°) (9)	V_{R_d} (km/s) (10)	V_last (km/s) (11)	R_last (kpc) (12)	Ref. (13)	$V_{R_\mathrm{d}}/R_\mathrm{d}$ (km/s/kpc) (14)
UGC 731	11.8±4.3	TF	a	-17.1±0.8	22.9±0.1	2.62	h	57±3	50±4	74±4	10.3	k	19±7
UGC 2455$^\alpha$	6.4±1.2	TF	a	-17.7±0.4	20.1±0.1	0.72	h	51±3	23±10	*61±4*	3.7	k	32±15
UGC 3371	21.9±4.9	TF	b	-18.6±0.4	23.2±0.1	5.58	h	49±3	51±3	86±3	17.4	k	9±2
UGC 3711	8.2±1.5	TF	a	-17.4±0.4	21.1±0.1	0.87	h	60±3	79±4	95±4	3.6	k	91±17
UGC 3817	8.3±3.1	TF	a	-14.8±0.8	22.7±0.1	0.64	h	30±3	16±5	*45±5*	2.4	k	25±12
UGC 3966	7.4±1.4	TF	a	-15.2±0.4	22.5±0.1	0.67	h	41±3	38±5	50±5	2.7	k	57±13
UGC 4173	16.7±3.1	TF	a	-17.7±0.4	24.1±0.1	4.97	h	40±3	36±5	*57±5*	12.2	k	7±2
UGC 4325	10.0±1.8	TF	a	-18.0±0.4	21.4±0.1	1.74	h	41±3	73±3	92±3	5.8	k	42±8
UGC 4499	12.8±2.4	TF	a	-17.7±0.4	21.8±0.1	1.33	h	50±3	38±4	74±3	8.4	k	29±6
UGC 4543	30.0±5.5	TF	a	-19.2±0.4	22.4±0.1	3.34	h	46±3	59±4	67±4	17.4	k	18±4
UGC 5272	6.5±1.2	TF	a	-15.2±0.4	22.0±0.1	0.68	h	59±3	19±4	*45±4*	1.9	k	28±8
UGC 5414	9.4±1.7	TF	a	-17.4±0.4	21.8±0.1	1.38	h	55±3	35±3	*61±2*	4.1	k	25±5
UGC 5721	5.9±1.1	TF	a	-16.3±0.4	20.3±0.1	0.39	h	61±3	39±3	79±3	6.4	k	100±20
UGC 5829	8.0±1.5	TF	a	-17.0±0.4	22.6±0.1	1.50	h	34±3	34±5	*69±5*	6.4	k	23±6
UGC 5846	19.3±3.6	TF	a	-16.9±0.4	22.8±0.1	1.77	h	30±3	30±6	51±6	5.6	k	17±5
UGC 5918	7.1±1.3	TF	a	-15.2±0.4	23.8±0.1	1.59	h	46±3	30±4	*45±4*	4.1	k	19±4
UGC 6399	18.4±3.0	TF	b	-18.0±0.3	22.3±0.2	2.14	i	75±2	53±7	88±5	8.0	l	26±5
UGC 6446	18.0±3.0	TF	b	-18.5±0.4	22.2±0.1	2.70	i	51±3	62±4	82±4	15.7	l	23±4
UGC 6955	16.1±2.7	TF	b	-18.1±0.4	23.0±0.1	3.91	h	64±2	49±3	82±2	15.6	m	12±2
UGC 7232	2.8±0.5	TF	a	-14.8±0.4	20.7±0.1	0.20	h	59±3	19±4	*44±4*	0.8	k	95±26
UGC 7261	7.9±1.5	TF	a	-17.3±0.4	22.0±0.1	1.34	h	30±3	66±6	76±6	4.0	k	49±11
UGC 7323	5.8±1.0	TF	b	-18.2±0.4	21.3±0.1	1.51	h	47±3	49±4	*86±4*	4.2	k	32±6
UGC 7524$^\beta$	4.3±0.4	Ceph	d	-18.6±0.2	22.1±0.1	2.82	h	46±3	58±4	79±4	9.7	k	21±3
UGC 7559	5.0±0.2	TRGB	e	-14.6±0.1	23.9±0.1	1.08	h	61±3	21±4	33±4	3.3	k	19±4
UGC 7577	2.6±0.1	TRGB	e	-15.0±0.1	22.4±0.1	0.64	h	63±3	8±3	*18±3*	1.7	k	12±5
UGC 7603	10.5±1.7	TF	b	-17.8±0.3	21.3±0.3	1.06	h	78±3	30±3	64±3	9.2	k	28±5
UGC 7690$^\gamma$	7.5±1.4	TF	a	-16.9±0.4	20.2±0.1	0.43	h	41±3	44±4	56±4	3.8	k	102±22

Table 5.B.3 – continued.

Name (1)	Dist (Mpc) (2)	Method (3)	Ref. (4)	$M_{\rm R}$ (mag) (5)	$\mu^{i}_{0,R}$ (mag/$''^{2}$) (6)	$R_{\rm d}$ (kpc) (7)	Ref. (8)	i (°) (9)	$V_{R_{\rm d}}$ (km/s) (10)	$V_{\rm last}$ (km/s) (11)	$R_{\rm last}$ (kpc) (12)	Ref. (13)	$V_{R_{\rm d}}/R_{\rm d}$ (km/s/kpc) (14)
UGC 7866	4.6±0.2	TRGB	e	-15.1±0.1	22.1±0.1	0.55	h	44±3	17±4	*33±4*	2.3	k	31±8
UGC 7916	7.2±2.6	TF	a	-14.6±0.8	24.4±0.2	1.47	h	74±3	21±3	*36±3*	3.7	k	14±5
UGC 7971	8.0±1.5	TF	a	-17.0±0.4	21.3±0.1	0.89	h	38±3	22±5	*45±5*	2.9	k	25±7
UGC 8320	4.6±0.2	TRGB	e	-15.9±0.1	22.3±0.1	0.79	h	61±3	21±4	49±4	4.0	m	27±5
UGC 8490^{γ}	4.6±0.6	TRGB	f	-17.2±0.3	20.4±0.1	0.65	h	50±3	48±4	78±4	10.0	k	74±12
UGC 8837	7.2±0.1	TRGB	e	-16.5±0.1	23.7±0.3	1.73	h	80±3	25±3	*48±4*	4.2	k	14±2
UGC 9211	14.7±2.7	TF	a	-16.5±0.4	22.7±0.1	1.38	h	44±3	35±4	65±4	9.6	k	25±6
UGC 9992	11.2±2.1	TF	a	-16.0±0.4	21.9±0.1	0.86	h	30±3	28±6	34±6	4.1	k	33±10
UGC 10310	15.8±2.9	TF	a	-17.9±0.4	21.9±0.1	1.91	h	34±3	44±5	74±5	9.2	k	23±5
UGC 11557	23.7±4.4	TF	a	-19.0±0.4	20.9±0.1	3.01	h	30±3	53±6	85±6	10.3	k	18±4
UGC 11707	15.7±3.0	TF	a	-18.2±0.4	23.1±0.2	4.41	h	68±3	68±7	100±3	15.0	k	15±3
UGC 12060	15.1±2.8	TF	a	-17.7±0.4	21.8±0.1	1.52	h	40±3	61±4	74±4	9.9	k	40±8
UGC 12632	9.2±1.7	TF	a	-17.5±0.4	23.3±0.1	3.78	h	46±3	58±4	76±3	11.4	k	15±3
UGC 12732	12.4±2.3	TF	a	-17.8±0.4	22.4±0.1	2.13	h	39±3	53±5	*98±5*	14.4	k	25±5
$\rm WLM^{\delta}$	1.0±0.1	Ceph	g	-14.1±0.2	22.5±0.2	0.57	j	70±4	19±2	*43±4*	3.7	n	33±5
NGC 6822^{δ}	0.5±0.1	Ceph	g	-15.0±0.4	21.3±0.1	0.57	j	59±3	20±1	56±3	4.7	o	35±7

Notes. $^{(\alpha)}$ the H I line profiles are very broad and complex; we assigned a larger error to $V_{R_{\rm d}}$ than given by Swaters et al. (2009).
$^{(\beta)}$ the galaxy is kinematically lopsided, but the H I kinematics is quite symmetric in the inner regions.
$^{(\gamma)}$ the H I disk is warped, the inclination is given for $R \simeq R_{\rm d}$.
$^{(\delta)}$ the V-band values from Hunter & Elmegreen (2006) have been converted to R-band assuming $V - R = 0.5$.

Table 5.B.4 – Sample of irregulars. Gas and star-formation properties. References:(a) Hunter & Hoffman (1999); (b) Berg et al. (2012); (c) van Zee & Haynes (2006); (d) Croxall et al. (2009); (e) Esteban et al. (2009); (f) Lee et al. (2005); (g) Swaters et al. (2002); (h) Verheijen & Sancisi (2001); (i) Broeils (1992); (j) Kepley et al. (2007); (k) Weldrake et al. (2003); (l) Kennicutt et al. (2008); (m) James et al. (2004).

Name (1)	log(O/H) +12 (2)	Ref. (3)	$M_{\rm H\,I}$ ($10^8 M_\odot$) (4)	$\overline{\Sigma}_{\rm H\,I}$ ($M_\odot$/pc^2) (5)	Ref. (6)	EW(Hα) (Å) (7)	SFR ($M_\odot$/yr) (8)	Ref. (9)	SFR/$M_{\rm bar}$ (Gyr^{-1}) (10)	log($\Sigma_{\rm SFR}$) ($M_\odot$/yr/kpc^2) (11)	$\tau_{\rm global}$ (Gyr) (12)	$\tau_{\rm local}$ (Gyr) (13)
UGC 731	*8.46±0.20*	a	16.1±11.8	5.5±0.7	g	...	...	...	...	...	...	...
UGC 2455	*8.39±0.20*	a	6.9±2.7	10.1±1.2	g	49±4	0.161	l	*0.247*	-2.01	5.7	1.4
UGC 3371	*8.48±0.20*	a	35.6±16.3	3.2±0.4	g	24±2	0.041	m	0.016	-4.39	115.5	104.0
UGC 3711	...	...	6.2±2.4	7.7±1.0	g	44±4	0.097	l	0.025	-2.40	8.5	2.6
UGC 3817	...	...	2.1±1.6	4.5±0.5	g	59±8	0.008	l	*0.041*	-3.22	34.9	9.9
UGC 3966	*8.15±0.20*	a	3.2±1.2	6.4±0.7	g	20±4	0.005	l	0.017	-3.46	85.1	24.6
UGC 4173	...	...	23.8±8.0	3.0±0.3	g	60±6	0.056	m	*0.113*	-4.15	56.5	56.5
UGC 4325	8.15±0.05	b	7.4±2.7	6.6±0.7	g	32±4	0.075	l	0.022	-3.11	12.9	11.4
UGC 4499	...	...	11.5±4.5	7.2±0.8	g	49±5	0.082	m	0.058	-2.84	18.6	6.6
UGC 4543	...	...	72.2±27.4	5.4±0.6	g	...	...	...	...	...	...	...
UGC 5272	7.87±0.05	b	1.9±0.7	8.9±1.2	g	45±4	0.016	l	*0.083*	-2.97	15.8	11.0
UGC 5414	...	...	5.7±2.1	6.0±0.7	g	49±5	0.051	m	*0.078*	-3.08	14.9	9.6
UGC 5721	*8.32±0.20*	a	5.1±2.0	11.7±1.6	g	53±4	0.037	l	0.020	-2.12	18.3	2.1
UGC 5829	*8.30±0.10*	c	8.8±3.4	6.7±0.7	g	38±4	0.049	l	*0.046*	-3.17	23.9	13.2
UGC 5846	...	...	15.3±5.9	5.1±0.5	g	...	...	...	...	...	...	...
UGC 5918	7.84±0.04	d	2.5±0.9	2.6±0.3	g	19±5	0.003	l	0.016	-4.43	110.8	93.7
UGC 6399	...	...	8.4±2.7	...	h	25±2	0.067	m	0.024	-3.34	16.7	...
UGC 6446	...	...	31.0±10.3	5.5±0.6	h	80±8	0.117	m	0.055	-3.30	35.2	14.7
UGC 6955	*8.26±0.20*	a	20.8±7.3	...	i	20±5	0.047	m	0.022	-4.02	58.9	...
UGC 7232	...	...	0.4±0.2	7.8±1.0	g	22±5	0.003	l	*0.017*	-2.63	17.7	4.4
UGC 7261	...	...	5.0±2.0	5.2±0.5	g	42±4	0.075	l	0.048	-2.89	8.9	5.3
UGC 7323	...	...	3.8±1.4	4.1±0.5	g	18±3	0.038	l	0.015	-3.29	13.3	10.5
UGC 7524	8.09±0.15	e	14.6±3.0	3.9±0.4	g	27±4	0.079	l	0.043	-3.51	24.6	16.8
UGC 7559	...	...	1.8±0.2	3.6±0.5	g	38±5	0.008	l	0.143	-3.67	29.9	22.5
UGC 7577	7.97±0.06	b	0.45±0.06	2.1±0.3	g	9±2	0.002	l	*0.405*	-3.82	29.9	18.4
UGC 7603	...	...	12.8±4.3	6.3±1.7	g	35±4	0.081	l	0.103	-2.65	21.0	3.7
UGC 7690	...	...	3.3±1.3	8.8±1.0	g	24±4	0.024	l	0.052	-2.39	18.3	2.9
UGC 7866	...	...	1.2±0.2	4.7±0.5	g	49±4	0.012	l	*0.215*	-2.91	13.3	5.1

Table 5.B.4 – continued.

Name (1)	log(O/H) +12 (2)	Ref. (3)	$M_{\rm H\,I}$ ($10^8 M_\odot$) (4)	$\overline{\Sigma}_{\rm H\,I}$ ($M_\odot$/pc^2) (5)	Ref. (6)	EW(Hα) (Å) (7)	SFR ($M_\odot$/yr) (8)	Ref. (9)	SFR/$M_{\rm bar}$ (Gyr^{-1}) (10)	log($\Sigma_{\rm SFR}$) ($M_\odot$/yr/kpc^2) (11)	$\tau_{\rm global}$ (Gyr) (12)	$\tau_{\rm local}$ (Gyr) (13)
UGC 7916	...	...	2.6±1.9	3.1±0.6	g	63±22	0.014	l	*0.177*	-3.70	24.7	20.5
UGC 7971	*8.43±0.20*	a	2.5±0.9	5.7±0.6	g	25±4	0.017	l	*0.088*	-3.18	19.6	11.4
UGC 8320	*8.29±0.20*	a	3.5±0.5	...	i	22±4	0.008	l	0.029	-3.40	58.2	...
UGC 8490	...	...	7.0±2.0	9.1±1.1	g	54±5	0.063	l	0.036	-2.33	14.8	2.6
UGC 8837	7.87±0.07	b	3.2±0.3	1.8±0.6	g	37±4	0.022	l	*0.088*	-3.64	19.3	10.5
UGC 9211	...	...	14.2±5.4	6.2±0.7	g	57±12	0.036	l	0.043	-3.23	52.5	14.0
UGC 9992	7.88±0.12	c	3.5±1.4	5.3±0.5	g	20±4	0.009	l	0.143	-3.42	51.7	18.6
UGC 10310	*8.31±0.20*	a	12.9±4.9	6.2±0.7	g	63±6	0.147	m	0.104	-2.90	11.7	6.6
UGC 11557	...	...	25.0±9.6	5.0±0.5	g	35±3	0.486	m	0.198	-2.78	6.8	4.0
UGC 11707	...	...	36.3±14.3	5.2±0.8	g	...	...	...	...	...	...	...
UGC 12060	*8.34±0.20*	a	16.7±6.4	4.0±0.4	g	...	...	...	...	...	...	...
UGC 12632	*8.34±0.20*	a	15.4±5.9	3.4±0.4	g	40±6	0.060	l	0.038	-3.88	34.1	34.6
UGC 12732	...	...	32.3±12.4	4.7±0.5	g	88±9	0.086	m	*0.020*	-3.23	49.9	10.6
WLM	7.83±0.06	b	0.7±0.1	...	j	25±9	0.002	l	*0.012*	-3.72	46.5	...
NGC 6822$^{\alpha}$	8.11±0.10	f	1.5±0.6	...	k	47±12	0.011	l	0.024	-2.98	18.1	...

Notes. $^{(\alpha)}$ Weldrake et al. (2003) do not provide the total H I flux, thus we used the single-dish value from Koribalski et al. (2004) to calculate $M_{\rm H\,I}$.

Table 5.B.5 – Sample of rotating spheroidals. We assumed a distance of 16.1±1.2 Mpc for all the galaxies. References: (a) van Zee et al. (2004a); (b) van Zee et al. (2004b).

Name (1)	M_R (mag) (2)	i (°) (3)	$\mu^i_{0,R}$ (mag/$''^2$) (4)	R_d (kpc) (5)	Ref. (6)	v_{R_d} (km/s) (7)	v_last (km/s) (8)	R_last (kpc) (9)	$\overline{\sigma}_\mathrm{obs}$ (km/s) (10)	Ref. (11)	V_{R_d} (km/s) (12)	V_last (km/s) (13)	$V_{R_\mathrm{d}}/R_\mathrm{d}$ (km/s/kpc) (14)
VCC 178	-16.6±0.2	60±3	20.9±0.1	0.52	a	14±3	30±3	1.1	46±5	b	48±5	73±7	92±12
VCC 437	-18.1±0.2	54±3	21.7±0.1	1.60	a	49±5	49±5	1.6	50±5	b	70±5	70±5	44±5
VCC 543	-17.9±0.2	62±3	21.6±0.1	1.23	a	35±4	46±4	1.6	44±5	b	56±5	68±5	45±5
VCC 990	-17.6±0.2	50±3	20.0±0.1	0.53	a	18±3	43±3	1.3	43±5	b	46±5	80±7	87±11
VCC 1036	-18.3±0.2	69±3	21.4±0.2	1.32	a	32±2	52±2	2.1	37±4	b	49±3	70±4	37±4
VCC 1122	-17.3±0.2	70±3	21.5±0.2	0.90	a	17±3	28±3	1.4	40±4	b	43±4	57±5	48±6
VCC 2019	-17.6±0.2	47±3	20.6±0.1	0.73	a	28±3	42±3	1.1	41±4	b	50±4	65±4	68±8
VCC 2050	-16.8±0.2	66±3	21.3±0.2	0.62	a	11±3	20±3	1.0	37±6	b	39±6	51±7	60±10

References

Aloisi, A., Clementini, G., Tosi, M., et al. 2007, ApJL, 667, L151

Aloisi, A., van der Marel, R. P., Mack, J., et al. 2005, ApJL, 631, L45

Annibali, F., Tosi, M., Aloisi, A., & van der Marel, R. P. 2011, AJ, 142, 129

Annibali, F., Tosi, M., Monelli, M., et al. 2009, AJ, 138, 169

Ashley, T., Simpson, C. E., & Elmegreen, B. G. 2013, AJ, 146, 42

Barnes, J. E. & Hernquist, L. 1996, ApJ, 471, 115

Bekki, K. 2008, MNRAS, 388, L10

Bekki, K. & Freeman, K. C. 2002, ApJL, 574, L21

Berg, D. A., Skillman, E. D., Marble, A. R., et al. 2012, ApJ, 754, 98

Binggeli, B. 1994, in European Southern Observatory Conference and Workshop Proceedings, Vol. 49, European Southern Observatory Conference and Workshop Proceedings, ed. G. Meylan & P. Prugniel, 13

Binggeli, B., Sandage, A., & Tammann, G. A. 1985, AJ, 90, 1681

Binney, J. & Tremaine, S. 1987, Galactic dynamics

Bono, G., Caputo, F., Marconi, M., & Musella, I. 2010, ApJ, 715, 277

Bothun, G. D., Mould, J. R., Caldwell, N., & MacGillivray, H. T. 1986, AJ, 92, 1007

Bournaud, F., Elmegreen, B. G., & Elmegreen, D. M. 2007, ApJ, 670, 237

Broeils, A. H. 1992, Dark and visible matter in spiral galaxies

Ciotti, L. 1991, A&A, 249, 99

Ciotti, L. & Bertin, G. 1999, A&A, 352, 447

Côté, P., Piatek, S., Ferrarese, L., et al. 2006, ApJS, 165, 57

Cox, A. L., Sparke, L. S., Watson, A. M., & van Moorsel, G. 2001, AJ, 121, 692

Croxall, K. V., van Zee, L., Lee, H., et al. 2009, ApJ, 705, 723

Davies, J. I. & Phillipps, S. 1988, MNRAS, 233, 553

de Vaucouleurs, G., de Vaucouleurs, A., Corwin, Jr., H. G., et al. 1991, Third Reference Catalogue of Bright Galaxies. Volume I: Explanations and references. Volume II: Data for galaxies between 0^h and 12^h. Volume III: Data for galaxies between 12^h and 24^h.

Dekel, A. & Birnboim, Y. 2006, MNRAS, 368, 2

Dekel, A. & Silk, J. 1986, ApJ, 303, 39

Dellenbusch, K. E., Gallagher, III, J. S., & Knezek, P. M. 2007, ApJL, 655, L29

Dellenbusch, K. E., Gallagher, III, J. S., Knezek, P. M., & Noble, A. G. 2008, AJ, 135, 326

Drozdovsky, I. O. & Karachentsev, I. D. 2000, A&AS, 142, 425

Drozdovsky, I. O., Schulte-Ladbeck, R. E., Hopp, U., Crone, M. M., & Greggio, L. 2001, ApJL, 551, L135

Ekta, Chengalur, J. N., & Pustilnik, S. A. 2006, MNRAS, 372, 853

Ekta, B., Pustilnik, S. A., & Chengalur, J. N. 2009, MNRAS, 397, 963

Elmegreen, B. G., Zhang, H.-X., & Hunter, D. A. 2012, ApJ, 747, 105

Elson, E. C., de Blok, W. J. G., & Kraan-Korteweg, R. C. 2010, MNRAS, 404, 2061

Elson, E. C., de Blok, W. J. G., & Kraan-Korteweg, R. C. 2011, MNRAS, 415, 323
Esteban, C., Bresolin, F., Peimbert, M., et al. 2009, ApJ, 700, 654
Ferguson, H. C. & Binggeli, B. 1994, A&ARv, 6, 67
Fraternali, F., van Moorsel, G., Sancisi, R., & Oosterloo, T. 2002, AJ, 123, 3124
Freeman, K. C. 1970, ApJ, 160, 811
Gallagher, III, J. S. & Hunter, D. A. 1987, AJ, 94, 43
García-Benito, R. & Pérez-Montero, E. 2012, MNRAS, 423, 406
Gatto, A., Fraternali, F., Read, J. I., et al. 2013, MNRAS, 433, 2749
Gentile, G., Angus, G. W., Famaey, B., Oh, S.-H., & de Blok, W. J. G. 2012, A&A, 543, A47
Gil de Paz, A. & Madore, B. F. 2005, ApJS, 156, 345
Gil de Paz, A., Madore, B. F., & Pevunova, O. 2003, ApJS, 147, 29
Gnedin, O. Y., Ostriker, J. P., & Tremaine, S. 2013, ArXiv e-prints
Halliday, C., Davies, R. L., Kuntschner, H., et al. 2001, MNRAS, 326, 473
Hoessel, J. G., Saha, A., & Danielson, G. E. 1998, AJ, 115, 573
Holmberg, E. 1950, Meddelanden fran Lunds Astronomiska Observatorium Serie II, 128, 1
Howley, K. M., Guhathakurta, P., van der Marel, R., et al. 2013, ApJ, 765, 65
Hunter, D. A. & Elmegreen, B. G. 2004, AJ, 128, 2170
Hunter, D. A. & Elmegreen, B. G. 2006, ApJS, 162, 49
Hunter, D. A. & Hoffman, L. 1999, AJ, 117, 2789
Immeli, A., Samland, M., Gerhard, O., & Westera, P. 2004, A&A, 413, 547
Izotov, Y. I. & Thuan, T. X. 1999, ApJ, 511, 639
Izotov, Y. I. & Thuan, T. X. 2002, ApJ, 567, 875
Jackson, D. C., Skillman, E. D., Cannon, J. M., & Côté, S. 2004, AJ, 128, 1219
Jacobs, B. A., Rizzi, L., Tully, R. B., et al. 2009, AJ, 138, 332
James, P. A., Shane, N. S., Beckman, J. E., et al. 2004, A&A, 414, 23
Karachentsev, I. D., Makarov, D. I., Sharina, M. E., et al. 2003, A&A, 398, 479
Kelson, D. D., Illingworth, G. D., Tonry, J. L., et al. 2000, ApJ, 529, 768
Kennicutt, R. C. & Evans, N. J. 2012, ARA&A, 50, 531
Kennicutt, Jr., R. C. 1989, ApJ, 344, 685
Kennicutt, Jr., R. C. 1998a, ARA&A, 36, 189
Kennicutt, Jr., R. C. 1998b, ApJ, 498, 541
Kennicutt, Jr., R. C., Lee, J. C., Funes, José G., S. J., Sakai, S., & Akiyama, S. 2008, ApJS, 178, 247
Kepley, A. A., Wilcots, E. M., Hunter, D. A., & Nordgren, T. 2007, AJ, 133, 2242
Kereš, D., Katz, N., Weinberg, D. H., & Davé, R. 2005, MNRAS, 363, 2
Koribalski, B. S., Staveley-Smith, L., Kilborn, V. A., et al. 2004, AJ, 128, 16
Kormendy, J. 1985, ApJ, 295, 73
Kormendy, J. & Bender, R. 2012, ApJS, 198, 2
Kormendy, J., Fisher, D. B., Cornell, M. E., & Bender, R. 2009, ApJS, 182, 216

Leaman, R., Venn, K. A., Brooks, A. M., et al. 2012, ApJ, 750, 33
Lee, H., Skillman, E. D., & Venn, K. A. 2005, ApJ, 620, 223
Lee, J. C., Gil de Paz, A., Tremonti, C., et al. 2009, ApJ, 706, 599
Lelli, F., Fraternali, F., & Verheijen, M. 2013, MNRAS
Lelli, F., Verheijen, M., Fraternali, F., & Sancisi, R. 2012a, A&A, 537, A72
Lelli, F., Verheijen, M., Fraternali, F., & Sancisi, R. 2012b, A&A, 544, A145
Leroy, A. K., Walter, F., Brinks, E., et al. 2008, AJ, 136, 2782
Lisker, T., Glatt, K., Westera, P., & Grebel, E. K. 2006, AJ, 132, 2432
Lisker, T., Grebel, E. K., Binggeli, B., & Glatt, K. 2007, ApJ, 660, 1186
López-Sánchez, A. R., Koribalski, B., van Eymeren, J., et al. 2010, in Astronomical Society of the Pacific Conference Series, Vol. 421, Galaxies in Isolation: Exploring Nature Versus Nurture, ed. L. Verdes-Montenegro, A. Del Olmo, & J. Sulentic, 65
Lotz, J. M., Miller, B. W., & Ferguson, H. C. 2004, ApJ, 613, 262
Marlowe, A. T., Meurer, G. R., & Heckman, T. M. 1999, ApJ, 522, 183
Martin, C. L. 1996, ApJ, 465, 680
Martin, C. L. 1998, ApJ, 506, 222
Martin, C. L. & Kennicutt, Jr., R. C. 2001, ApJ, 555, 301
Mateo, M. L. 1998, ARA&A, 36, 435
Mayer, L. 2011, in EAS Publications Series, Vol. 48, EAS Publications Series, ed. M. Koleva, P. Prugniel, & I. Vauglin, 369–381
Mayer, L., Mastropietro, C., Wadsley, J., Stadel, J., & Moore, B. 2006, MNRAS, 369, 1021
McGaugh, S. S. 2012, AJ, 143, 40
McGaugh, S. S. & Wolf, J. 2010, ApJ, 722, 248
McQuinn, K. B. W., Skillman, E. D., Cannon, J. M., et al. 2010a, ApJ, 721, 297
McQuinn, K. B. W., Skillman, E. D., Cannon, J. M., et al. 2010b, ApJ, 724, 49
McQuinn, K. B. W., Skillman, E. D., Dalcanton, J. J., et al. 2012, ApJ, 759, 77
Meurer, G. R., Mackie, G., & Carignan, C. 1994, AJ, 107, 2021
Meurer, G. R., Staveley-Smith, L., & Killeen, N. E. B. 1998, MNRAS, 300, 705
Micheva, G., Östlin, G., Bergvall, N., et al. 2013, MNRAS, 431, 102
Minchev, I., Famaey, B., Combes, F., et al. 2011, A&A, 527, A147
Moore, B., Lake, G., & Katz, N. 1998, ApJ, 495, 139
Noeske, K. G., Guseva, N. G., Fricke, K. J., et al. 2000, A&A, 361, 33
Oh, S.-H., de Blok, W. J. G., Brinks, E., Walter, F., & Kennicutt, Jr., R. C. 2011, AJ, 141, 193
Ott, J., Walter, F., & Brinks, E. 2005a, MNRAS, 358, 1423
Ott, J., Walter, F., & Brinks, E. 2005b, MNRAS, 358, 1453
Papaderos, P., Izotov, Y. I., Thuan, T. X., et al. 2002, A&A, 393, 461
Papaderos, P., Loose, H.-H., Fricke, K. J., & Thuan, T. X. 1996, A&A, 314, 59
Rafikov, R. R. 2001, MNRAS, 323, 445
Roychowdhury, S., Chengalur, J. N., Begum, A., & Karachentsev, I. D. 2009,

MNRAS, 397, 1435

Sánchez-Janssen, R., Méndez-Abreu, J., & Aguerri, J. A. L. 2010, MNRAS, 406, L65

Sandage, A. & Hoffman, G. L. 1991, ApJL, 379, L45

Schulte-Ladbeck, R. E., Hopp, U., Greggio, L., Crone, M. M., & Drozdovsky, I. O. 2001, AJ, 121, 3007

Schwartz, C. M. & Martin, C. L. 2004, ApJ, 610, 201

Sérsic, J. L. 1963, Boletin de la Asociacion Argentina de Astronomia La Plata Argentina, 6, 41

Simpson, C. E. & Gottesman, S. T. 2000, AJ, 120, 2975

Spolaor, M., Hau, G. K. T., Forbes, D. A., & Couch, W. J. 2010, MNRAS, 408, 254

Swaters, R. A. & Balcells, M. 2002, A&A, 390, 863

Swaters, R. A., Sancisi, R., van Albada, T. S., & van der Hulst, J. M. 2009, A&A, 493, 871

Swaters, R. A., van Albada, T. S., van der Hulst, J. M., & Sancisi, R. 2002, A&A, 390, 829

Tammann, G. A. 1994, in European Southern Observatory Conference and Workshop Proceedings, Vol. 49, European Southern Observatory Conference and Workshop Proceedings, ed. G. Meylan & P. Prugniel, 3

Taylor, C. L., Kobulnicky, H. A., & Skillman, E. D. 1998, AJ, 116, 2746

Terlevich, R., Melnick, J., Masegosa, J., Moles, M., & Copetti, M. V. F. 1991, A&AS, 91, 285

Thim, F., Hoessel, J. G., Saha, A., et al. 2004, AJ, 127, 2322

Tolstoy, E., Hill, V., & Tosi, M. 2009, ARA&A, 47, 371

Tolstoy, E., Saha, A., Hoessel, J. G., & McQuade, K. 1995, AJ, 110, 1640

Toomre, A. 1964, ApJ, 139, 1217

Tosi, M., Sabbi, E., Bellazzini, M., et al. 2001, AJ, 122, 1271

Tully, R. B. 1988, Nearby galaxies catalog

Tully, R. B., Rizzi, L., Shaya, E. J., et al. 2009, AJ, 138, 323

Tully, R. B., Verheijen, M. A. W., Pierce, M. J., Huang, J.-S., & Wainscoat, R. J. 1996, AJ, 112, 2471

van Eymeren, J., Koribalski, B. S., López-Sánchez, Á. R., Dettmar, R.-J., & Bomans, D. J. 2010, MNRAS, 407, 113

van Eymeren, J., Marcelin, M., Koribalski, B., et al. 2009a, A&A, 493, 511

van Eymeren, J., Marcelin, M., Koribalski, B. S., et al. 2009b, A&A, 505, 105

van Zee, L. 2001, AJ, 121, 2003

van Zee, L., Barton, E. J., & Skillman, E. D. 2004a, AJ, 128, 2797

van Zee, L. & Haynes, M. P. 2006, ApJ, 636, 214

van Zee, L., Salzer, J. J., & Skillman, E. D. 2001, AJ, 122, 121

van Zee, L., Skillman, E. D., & Haynes, M. P. 2004b, AJ, 128, 121

van Zee, L., Skillman, E. D., & Salzer, J. J. 1998, AJ, 116, 1186

Verheijen, M. A. W. 2001, ApJ, 563, 694

Verheijen, M. A. W. & Sancisi, R. 2001, A&A, 370, 765
Weijmans, A.-M., Krajnović, D., van de Ven, G., et al. 2008, MNRAS, 383, 1343
Weisz, D. R., Dalcanton, J. J., Williams, B. F., et al. 2011, ApJ, 739, 5
Weisz, D. R., Skillman, E. D., Cannon, J. M., et al. 2008, ApJ, 689, 160
Weldrake, D. T. F., de Blok, W. J. G., & Walter, F. 2003, MNRAS, 340, 12